











Electronic states of metallic electric toroidal quadrupole order in $\text{Cd}_2\text{Re}_2\text{O}_7$ determined by combining quantum oscillations and electronic structure calculations

Hishiro T. Hirose ^{1,*}, Taichi Terashima ², Daigorou Hirai ³, Yasuhito Matsubayashi ^{3,†}, Naoki Kikugawa ⁴,
David Graf ⁵, Kaori Sugii ^{3,‡}, Shiori Sugiura ^{2,§}, Zenji Hiroi ³, and Shinya Uji ¹

¹Research Center for Functional Materials, National Institute for Materials Science, Tsukuba, Ibaraki 305-0003, Japan

²International Center for Materials Nanoarchitectonics, National Institute for Materials Science, Tsukuba, Ibaraki 305-0003, Japan

³Institute for Solid State Physics, University of Tokyo, Kashiwa, Chiba 277-8581, Japan

⁴Center for Green Research on Energy and Environmental Materials, National Institute for Materials Science, Tsukuba, Ibaraki 305-0003, Japan

⁵National High Magnetic Field Laboratory, Florida State University, Tallahassee, Florida 32310, USA



(Received 17 May 2021; revised 26 September 2021; accepted 17 December 2021; published 10 January 2022)

Pyrochlore oxide $\text{Cd}_2\text{Re}_2\text{O}_7$ exhibits successive structural transitions upon cooling that break its inversion symmetry. The low-temperature noncentrosymmetric metallic phases are believed to be some odd-parity multipole ordered states that are associated with a Fermi-liquid instability due to the strong spin-orbit interaction (SOI) and electronic correlation. However, their microscopic ordering pictures and the driving force of the phase transitions are still unclear. We determined the electronic structure of the lowest temperature phase of $\text{Cd}_2\text{Re}_2\text{O}_7$ by combining quantum oscillation measurements with electronic structure calculations. The observed Fermi surfaces were well reproduced based on the optimized crystal structure, and we demonstrated the strong influence of the antisymmetric SOI. From the mass enhancement factor, we elucidated the strongly correlated nature of the electronic states. In addition, we visualized the microscopic picture of the $3z^2 - r^2$ -type metallic electric-toroidal-quadrupole (ETQ) order characterized by the Re-O bond order. These results corroborate that the metallic ETQ order is driven by a Fermi-liquid instability associated with the strong SOI and electronic correlation, as has been theoretically proposed. Our results provide the basis for exploring unconventional phenomena expected in the metallic ETQ order.

DOI: [10.1103/PhysRevB.105.035116](https://doi.org/10.1103/PhysRevB.105.035116)

I. INTRODUCTION

Fermi-liquid instability associated with the strong spin-orbit interaction and electronic correlation has attracted considerable interest in condensed matter physics [1,2]. It is theoretically expected that the instability induces an inversion symmetry breaking order, such as an odd-parity multipole order in the metallic state [3]. In such a system, a multipole moment associated with Fermi surface (FS) splitting in the momentum space induces various off-diagonal responses such as the magnetocurrent effect [4–6]; in other words, the momentum-dependent spin polarizations on spin-split FSs respond to external fields as if there were multipole moments. Furthermore, it is also expected that the fluctuation of the inversion symmetry breaking order can lead to unconventional superconductivities [7–11]. The pyrochlore

oxide superconductor $\text{Cd}_2\text{Re}_2\text{O}_7$ is a promising candidate compound [12].

$\text{Cd}_2\text{Re}_2\text{O}_7$ shows successive structural transitions with decreasing temperature. Above $T_{s1} \sim 200$ K, $\text{Cd}_2\text{Re}_2\text{O}_7$ crystallizes in a centrosymmetric cubic structure (phase I: $Fd\bar{3}m$) where the Re atom is coordinated by six $\text{O}(1_I)$ atoms and makes the pyrochlore network that is interpenetrated by the $\text{CdO}(2_I)$ zincblende network [see Fig. 1(a); the subscript “I” of the oxygen site numbers indicates the notation for phase I] [13]. At T_{s1} , a second-order structural transition to a noncentrosymmetric tetragonal structure (phase II: $I\bar{4}m2$) occurs [14]. Despite the minimal lattice distortion [14,15], the results of resistivity, magnetic susceptibility, Hall coefficient, and NMR measurements corroborate a drastic change of electronic states at T_{s1} [16–20]. Thus, the transition is thought to be an electronic origin, similar to the band Jahn–Teller transition [21] or the electronic nematic transition [22,23]. At $T_{s2} \sim 115$ K, a first-order structural transition to another noncentrosymmetric tetragonal structure (phase III: $I4_122$) occurs [14,24]. Considering both $I\bar{4}m2$ and $I4_122$ are subgroups of $Fd\bar{3}m$ and the transition between phases II and III is of the first order, they are likely competing [25]. Recently, a next second-order structural transition to a noncentrosymmetric orthorhombic structure (phase IV: $F222$) at $T_{s3} \sim 80$ K was observed in Raman spectra [26]. Because this transition has not been discernible in other experiments [12] and the symmetry of phase IV is inconsistent with other experiments

*Present address: National Institute of Advanced Industrial Science and Technology, Tsukuba, Ibaraki 305-8564, Japan; hishirose@gmail.com

†Present address: National Institute of Advanced Industrial Science and Technology, Tsukuba, Ibaraki 305-8564, Japan.

‡Present address: National Institute of Advanced Industrial Science and Technology, Tsukuba, Ibaraki 305-8560, Japan.

§Present address: Institute for Materials Research, Tohoku University, Sendai, Miyagi 980-8577, Japan.

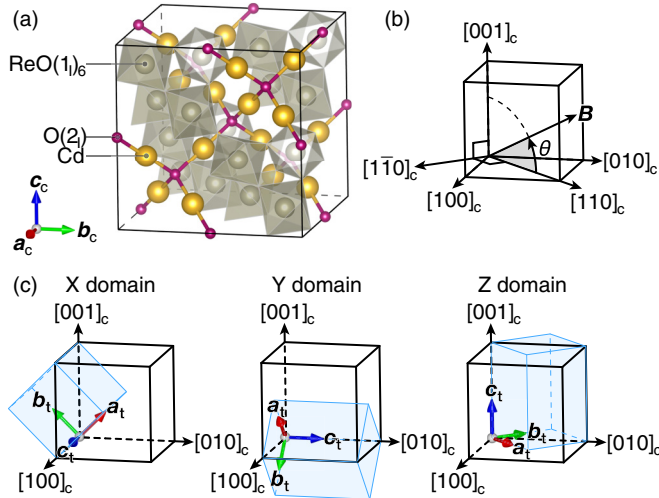


FIG. 1. (a) Crystal structure of $\text{Cd}_2\text{Re}_2\text{O}_7$ in a conventional unit cell in phase I, which is drawn using VESTA [32]. (b) The notation for θ in a cubic conventional unit cell in phase I. (c) Tetragonal conventional unit cells (azure part) in phase III for the X, Y, and Z domains displayed in a cubic conventional unit cell (black line) in phase I.

[14,27–29], the symmetry reduction to $F222$ in low temperatures is still controversial. Finally, $\text{Cd}_2\text{Re}_2\text{O}_7$ exhibits superconducting transition at $T_c = 0.97$ K [12,30,31].

Based on the lattice symmetries, Ref. [6] theoretically proposed that phases II and III are described by electric (axial) toroidal quadrupoles (ETQs) with $x^2 - y^2$ and $3z^2 - r^2$ components, respectively, which are illustrated in Fig. 2. For ease of understanding, we also show their corresponding spherical harmonic representations. ETQs are multipoles comprising electric toroidal moments, and each electric toroidal moment is described by the toroidal (circular) charge arrangement. Because space inversion reverses the signs of these ETQs, they are types of odd-parity multipoles (note that the spherical

	Electric toroidal quadrupole	Spherical harmonic representation
$x^2 - y^2$		
$3z^2 - r^2$		

FIG. 2. Electric toroidal quadrupoles of $x^2 - y^2$ and $3z^2 - r^2$ types are shown together with the spherical harmonic representations. The small green arrows represent the electric dipoles, whereas the large blue arrows represent the electric toroidal dipoles.

harmonic representations do not reverse the sign). Experimentally, magnetic torque (τ) measurement have proposed a coexistence between the ETQ and electric quadrupole orders in phases II and III [29,33]. By contrast, second harmonic generation studies suggest the possibilities of magnetic multipoles and ETQ orders in phase II [34–36]. Therefore, the nature of multipole orders is still under debate, and an identification of these orders is strongly demanded.

The determination of the electronic states in the ordered phases is thus a crucial issue in $\text{Cd}_2\text{Re}_2\text{O}_7$. Though the electronic states probably play a key role in the phase transitions, those in the ordered states have not yet been clarified. Consequently, the microscopic picture of the orders that arise in the metallic state remains unclear. Corresponding to the spin splitting of FSs in the momentum space, a certain order should exist in the real space that is coupled to the crystal structure. Because these changes in momentum and real spaces are in correspondence, it is important to identify them simultaneously. These results will provide indirect evidence of the multipole order. In addition, insights into the electronic states are indispensable to discuss the source of the energy stabilization in the ordered phases. Furthermore, the quantitative estimation of the predicted phenomena, such as the magnetocurrent effect, requires information of the FSs because they are sensitive to the electronic states at the Fermi level (E_F).

Our previous quantum oscillation measurements on $\text{Cd}_2\text{Re}_2\text{O}_7$ using τ showed complex frequency branches and large cyclotron effective masses up to $9m_e$ (m_e is a free electron mass) [37]. The angular dependence of the frequencies was interpreted as part of the six spin-split FSs, calculated based on the reported structural parameters taken at 90 K [38]. However, τ is sensitive only to the anisotropy of the FS, which limits the observation of quantum oscillations from the nearly isotropic part of the FSs. In addition, a large discrepancy exists between the experimental results and the calculation. There are two main reasons for this: One is that the crystal structure parameters change with temperature, and the reported structure may not match the one at the lowest temperature at which we measured the quantum oscillations. The other reason is that the FSs are sensitive to the strength of the electronic correlations considered in the calculation, and the strength is still controversial [12,17,19,38].

In the present study, we performed a complementary measurement of quantum oscillations on the AC magnetic susceptibility (χ_{AC}) and electrical conductivity (σ). As shown later, quantum oscillations in different physical quantities exhibit different amplitudes, allowing us to identify new frequencies and trace individual branches. In addition, we succeeded in reproducing the quantum oscillation spectra much more accurately than in Ref. [37] by refining the conditions we used to calculate the electronic states; more specifically, we employed a structural optimization while tuning the strength of the electronic correlation. This enables a discussion based on the electronic structure.

II. METHODS

A. Experiments

Single crystals of $\text{Cd}_2\text{Re}_2\text{O}_7$ were grown by the chemical vapor transport method, as described in Ref. [20]. The

quantum oscillations on the χ_{AC} were measured using a standard field modulation method [39]. The modulation field B_{mod} of 0.01 T and 67.1 Hz was applied on a 1 mm³ size single crystal placed in a pickup coil with the [111]_c axis (subscript ‘‘c’’ denotes the notation in the cubic unit cell) parallel to the coil axis. The second harmonic signal of the coil voltage (v), which roughly corresponds to $d\chi_{AC}/dB$, was obtained using standard lock-in acquisition. The measurement was performed in a dilution refrigerator equipped with a 20 T superconducting magnet. The quantum oscillations on the σ were measured by employing a standard four-probe method, which was conducted in a ³He refrigerator with a 32 T resistive magnet at NHMFL. These data were analyzed together with the previous τ data [37]. In all measurements, the samples were rotated around the [1 $\bar{1}$ 0]_c direction in the magnetic field, and the field angle θ was measured from the [110]_c direction, as illustrated in Fig. 1(b). The measurement temperatures for the v , σ , and τ are 40 mK, 0.5 K, and 30 mK, respectively, except for the temperature dependence measurements.

We analyzed the quantum oscillations based on the $I4_122$ space group symmetry (phase III) because the symmetry reduction from $I4_122$ to $F222$ is ‘‘almost’’ imperceptible in our data. In phase III, three types of tetragonal domains, X, Y, and Z domains, are formed, whose c_t axes (subscript ‘‘t’’ denotes the notation in the tetragonal unit cell) lie along the [100]_c, [010]_c, and [001]_c directions, respectively, as shown in Fig. 1(c). The observed quantum oscillations include all signals from the three domains. Because B is confined within the (1 $\bar{1}$ 0)_c plane, signals from the X and Y domains are equivalent. In addition, when $B \parallel [111]_c$, the signals from all domains are equivalent. Note that in $F222$, the X, Y, and Z domains are further split into two different domains for each, although that was imperceptible in the polarizing microscopy experiment [28].

Based on the Lifshitz-Kosevich formula, a quantum oscillation measured on a physical quantity q (v , σ , and τ) is expressed as follows:

$$\frac{\tilde{q}}{|q|} = C f_q |S''|^{-1/2} R_T R_D \sin \left[2\pi \left(\frac{F}{B} - \frac{1}{2} \right) \pm \frac{\pi}{4} \right], \quad (1)$$

where C is a constant, and $S'' = \partial^2 S / \partial k_{\parallel B}^2$ is the curvature factor [39]. The higher harmonics, Zeeman effect, and Berry’s phase are neglected. The \pm sign is positive (negative) for the minimum (maximum) cross-sectional area S of the FS perpendicular to B , which is related to frequency F , as $F = \hbar S / 2\pi e$. The temperature and Dingle reduction factors are given by $R_T = \xi / \sinh \xi$ and $R_D = \exp(-\xi_D)$, respectively, where $\xi_{(D)} = 2\pi^2 k_B T_{(D)} m^* / e \hbar B$, T_D is the Dingle temperature, m^* is the cyclotron effective mass, and k_B is the Boltzmann constant. The factor f_q is different for each physical quantity and is expressed as $f_v = (\cos \phi - \frac{1}{F} \frac{\partial F}{\partial \phi} \sin \phi) J_2(\lambda) F B^{1/2} / m^*$ for the field modulation technique with the second-harmonic detection, $f_\sigma = B^{1/2} m^*$ for electrical conductivity, assuming a uniform scattering rate on FSs, and $f_\tau = (\partial F / \partial \theta) B^{3/2} / m^*$ for magnetic torque. Here, J_2 is a second-order Bessel function, $\lambda = 2\pi F B_{\text{mod}} / B^2$, and ϕ is the angle between B and the pickup coil axis. Because of f_q , the relative

amplitude of each frequency depends on the measurement method.

B. Calculations

The fully relativistic electronic structure was calculated based on the rotationally invariant DFT + U method using the screened Coulomb and exchange parameters [40] as implemented in the QUANTUM ESPRESSO package [41]. Fully relativistic optimized norm-conserving Vanderbilt pseudopotentials generated using the code ONCVSP [42–45] were used with the Perdew, Burke, and Ernzerhof (PBE) type exchange potential [46] and a plane-wave cutoff energy of 100 Ry. A 10^3 k -point mesh was used for the self-consistent field procedure, whereas a 16^3 k -point mesh was used to calculate the density of states (DOS). The atomic positions were optimized until the change in the total energy became less than 10^{-6} eV. The FSs were calculated using the 24-orbital tight-binding model based on maximally localized Wannier functions constructed with the WANNIER90 program [47]. The quantum oscillation frequencies were simulated using the algorithm described in Ref. [48].

It is not appropriate to entirely rely on experimental crystal structures because they may depend on temperature, as noted later. In addition, the optimal screened Coulomb parameter U depends on the materials and pseudopotentials [49]; therefore, it is not known *a priori*. Thus, we employed a round-robin method to obtain electronic states that were as close as possible to those experimentally observed by quantum oscillations; we optimized all the independent internal atomic coordinates in phase III with various values of U and the screened exchange parameter J at the Re site. We found that the result with $U = 4.5$ eV gives the simulated quantum oscillation frequencies closest to the experiment, whereas the dependence on J is minimal; thus, we used a typical value of $J = 0.3$ eV (see Appendix A for details).

In the calculations, we fixed the lattice constants to those of phase I ($a_c = 10.2382$ Å), which was optimized together with an internal coordinate using the above U and J values. This was done for three reasons: First, the reported lattice distortion ratios in phase III (0.044% [50] and 0.016% [38]) are smaller than the calculation error of optimizing the lattice constants ($\sim 1\%$). Second, the fixed lattice constant facilitates the comparison of the charge density between phases I and III. Finally, the lattice distortion is so small that the effect of the lattice distortion is imperceptible in the calculated FSs and the simulated quantum oscillation spectra. This indicates that the lattice distortion itself is not essential for the electronic states and may appear as a side effect of the atomic displacements. Thus, we ignored the lattice distortion and focused on the atomic displacements.

During the structural optimization of phase III, we constrained the symmetry to $I4_122$. However, even if we attempted the structural optimization of phase IV ($F222$) using the same U and J values and starting from the optimized phase III structure, the symmetry reduction from $I4_122$ to $F222$ was negligible; the violation of the $I4_122$ symmetry in terms of the displacement of atomic coordinates was less than 0.00005. Thus, we ignored the symmetry reduction to $F222$ in our calculation.

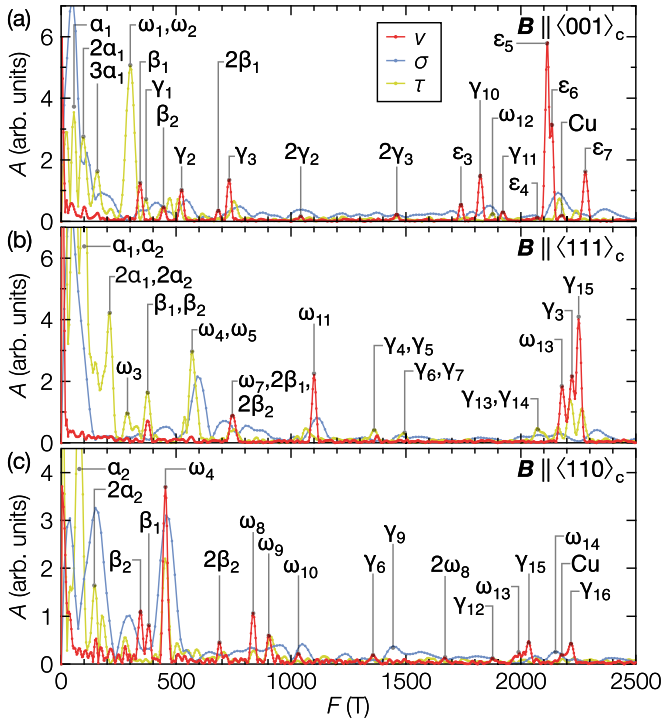


FIG. 3. (a) Fourier-transformed spectra measured on three different quantities (v , σ , and τ) for the magnetic fields along the $\langle 001 \rangle_c$, (b) $\langle 111 \rangle_c$, and (c) $\langle 110 \rangle_c$ directions. The field ranges for the Fourier transformation are 6.4–17.6 T, 17–32 T, and 10–17.5 T for AC magnetic susceptibility, electrical conductivity, and magnetic torque [37], respectively.

III. RESULTS

A. Quantum oscillations

1. Fourier-transformed spectra for major axes

Figure 3 shows the Fourier-transformed spectra of the quantum oscillations for the fields along the $\langle 001 \rangle_c$, $\langle 111 \rangle_c$, and $\langle 110 \rangle_c$ directions measured on the AC magnetic susceptibility, electrical conductivity, and magnetic torque. Clearly, the relative amplitudes of the quantum oscillation frequencies differ among the physical quantities. We observed several new peaks that were not observed in the previous study [37] and labeled all peaks according to their origins (described later). Note that we revised the branch names used in Ref. [37] because the number of Greek letters is short of naming all observed branches. The masses of the major peaks were obtained by fitting the temperature dependence of their amplitudes with the R_T function. All major peaks are summarized in Table I along with their corresponding frequency and mass.

2. Angular dependence of frequencies

The Fourier-transformed spectra as a function of field direction are plotted as color images in Figs. 4(a), 4(b), and 4(c) for the AC magnetic susceptibility, electrical conductivity, and magnetic torque, respectively. The AC magnetic susceptibility with the field modulation technique is effective in visualizing numerous branches, including those with small angular dependence, whereas it has a disadvantage in detecting small frequencies owing to the $J_2(\lambda)F$ factor in f_v . In the electrical

conductivity, the branches with heavy effective masses tend to show relatively large amplitudes compared to the case of other physical quantities owing to the m^* factor in f_σ . This enabled us to observe the ω_7 , δ_1 , ω_{11} , γ_9 , and ω_{14} branches that cannot be clearly observed with the other methods. Magnetic torque has its strength (weakness) in observing highly (weakly) anisotropic branches because of the $\partial F/\partial \theta$ factor in f_τ . The fundamental frequencies observed for the three methods are shown in Fig. 4(d). We connected all frequencies belonging to the same branch with the aid of intensity variation.

3. Assignment of branches to orbits on the Fermi surfaces

To assign the observed branches to the orbits on FSs, we simulated the quantum oscillation frequencies based on the calculated electronic states of phase III. The simulated angular dependence of the Fourier-transformed spectra using a typical $f_q = B^{1/2}/m^*$ is shown in Figs. 4(e) and 4(f) as colored images. Here, the deeper color corresponds to the larger amplitude, as indicated in the color scales shown at the bottom, and we used different colors for branches derived from each FS. The more specific simulations using f_v , f_σ , and f_τ are provided in Appendix B. The simulated spectra are largely different compared to the previously reported [37].

The calculated FSs and corresponding orbits are represented in Fig. 5 for the two orientations corresponding to the Z and X domains. The calculated FSs consist of six FSs: two hole FSs (FS7 and FS8) and four electron FSs (FS9, FS10, FS11, and FS12). We named these FSs after the index of the bands in the Re $5d t_{2g}$ manifold. The FSs are strongly different from the previously reported [37]. FS7 consists of a small double-conical-shaped pocket at the Z point and even smaller spherical pockets at the X point. The FS8 comprises a large pocket at the Z point and a bumpy cylinder extending along the c_1 axis. The FS9 to FS12 are located around the Γ point; the FS10 to FS12 are roughly spherical, while the FS9 has an extra part similar to crowns developing up and down.

Supported by the simulation, we assigned the observed branches to the orbits on the FSs as follows [see Fig. 4(d)]: The α_1 and α_2 branches coincide at $B \parallel [111]_c$, and thus, they are from the cross sections of the same part of an FS in different domains. Because they nearly diverge as $F \propto 1/\cos \theta$ or $F \propto 1/\cos(90^\circ - \theta)$, they correspond to the minimum orbit on the double-conical-shaped pocket of FS7 surrounding the Z point. Similarly, the nearly flat β_1 and β_2 branches originate from cross sections of the spherical FS12.

The angular dependence of the frequencies and the intensities of the γ_{1-18} branches are almost consistent with the simulation for FS8. Particularly, the γ_1 , γ_2 , γ_{4-7} , γ_{11} , and γ_{12} branches corresponding to the large pocket around the Z point were quantitatively well reproduced in the simulation. These branches were not reproduced in Ref. [37] because they are sensitive to the value of U and only appear when U is close to 4.5 eV, as shown in Appendix A. Note that the pair of branches $\{\gamma_3, \gamma_{15}\}$ arises from cross sections of the same part of the FS8 in the different domains because they coincide at $B \parallel [111]_c$; similarly, $\{\gamma_4, \gamma_5\}$, $\{\gamma_6, \gamma_7\}$, $\{\gamma_{11}, \gamma_{12}\}$, $\{\gamma_{13}, \gamma_{14}\}$, and $\{\gamma_{17}, \gamma_{18}\}$ branches are pairs.

TABLE I. Experimental and calculated parameters of the FSs in phase III.

Field direction	Branch	Experiment		Calculation					
		F (T)	m^*/m_e	Domain	FS	F (T)	m_b/m_e	S''	m^*/m_b
(001) _c	α_1^a	51	0.99(3)	Z	FS7	17	0.259	+0.765	3.8(1)
	ω_1^{ab}	287	2.4(1)						
	ω_2^{ab}	313	2.7(1)						
	β_1	342	2.6(1)	X, Y	FS12	251	0.462	-3.958	5.6(3)
	γ_1^a	369	3.4(3)	Z	FS8	204	0.855	+46.338	4.0(3)
	β_2	446	3.1(2)	Z	FS12	404	0.729	-8.345	4.2(3)
	δ_2			X, Y	FS11	455	1.019	-3.424	
	γ_2	523	4.6(2)	Z	FS8	486	1.492	-19.380	3.1(1)
	γ_3	731	5.4(2)	Z	FS8	1037	1.088	+8.507	4.9(1)
	δ_1			Z	FS11	885	0.950	-25.468	
	ζ_1			Z	FS10	1287	0.780	+0.446	
	ε_3	1740	6.3(4)	Z	FS9	2258	2.771	+24.902	2.3(1)
	ζ_2			X, Y	FS10	1793	1.043	-6.004	
	γ_{10}	1824	5.6(1)	Z	FS8	2072	2.163	-24.702	2.58(5)
	ω_{12}^a	1875	11.0(25)						
	γ_{11}	1921		X, Y	FS8	1839	3.513	-18.331	
	ε_4	2072		Z	FS9	2323	6.038	+97.817	
	ε_5	2113	5.41(3)	X, Y	FS9	2332	1.986	-1.660	2.72(2)
	ε_6	2134		Z	FS9	2360	1.653	+3.243	
	ε_7	2280	6.2(1)	Z	FS9	2406	1.914	-11.383	3.26(5)
(111) _c	α_1, α_2^a	106	1.77(3)	X, Y, Z	FS7	34	0.540	+6.708	3.28(5)
	ω_3^a	285	2.4(2)	X, Y, Z					
	β_1, β_2	373	3.0(2)	X, Y, Z	FS12	291	0.586	-4.606	5.1(4)
	δ_1, δ_2			X, Y, Z	FS11	528	0.948	-7.911	
	ω_4, ω_5^a	570	4.57(5)	X, Y, Z					
	ω_7	745	6.6(3)	X, Y, Z					
	ω_{11}	1100	7.5(2)	X, Y, Z					
	γ_4, γ_5	1361		X, Y, Z	FS8	1284	2.616	-4.247	
	γ_6, γ_7	1489		X, Y, Z	FS8	1427	3.490	-19.915	
	ζ_1, ζ_2			X, Y, Z	FS10	1642	1.103	-3.115	
	γ_{13}, γ_{14}	2070		X, Y, Z	FS8	2387	2.863	+15.523	
	ω_{13}	2180	7.5(1)	X, Y, Z					
	γ_3^c	2220	7.6(1)	Z	FS8	2414	3.030	-8.864	2.50(4)
	γ_{15}^c	2250	7.94(8)	X, Y	FS8	2414	3.030	-8.864	2.62(3)
(110) _c	α_2^a	74		X, Y	FS7	26	0.395	+2.460	
	β_2	342	2.5(2)	Z	FS12	248	0.489	-2.545	5.2(3)
	β_1	379	3.3(3)	X, Y	FS12	319	0.638	-6.242	5.1(5)
	ω_4	453	3.31(7)						
	δ_1			Z	FS11	499	0.955	-7.785	
	δ_2			X, Y	FS11	526	0.966	-4.475	
	ω_8	835	4.5(2)						
	ω_9	902	6.4(5)						
	ω_{10}	1029	4.4(7)						
	γ_6	1355		X, Y	FS8	1255	3.673	+1.499	
	γ_9	1440		X, Y	FS8	1815	2.371	-14.004	
	ζ_2			X, Y	FS10	1831	2.471	-34.839	
	γ_{12}	1875		Z	FS8	1827	3.089	-10.890	
	ω_{13}	1992							
	ζ_1			Z	FS10	1929	2.238	-26.553	
	γ_{15}	2032	6.3(4)	X, Y	FS8	2343	2.699	-11.123	2.3(2)
ω_{14}	2140								
γ_{16}	2217	6.2(3)	X, Y	FS8	2506	2.295	+0.609	2.7(2)	

^aExperimental data for these branches were obtained using magnetic torque data, whereas the others were obtained from the AC magnetic susceptibility data except for ω_{14} , which is from the electrical conductivity data.

^bThese two branches coincide at $B \parallel [001]_c$. Because the effective masses of the torque data were measured slightly away from $[001]_c$, they split into two peaks.

^cThese two branches are expected to coincide at $B \parallel [111]_c$. They split into two peaks probably because of the to misalignment of the sample.

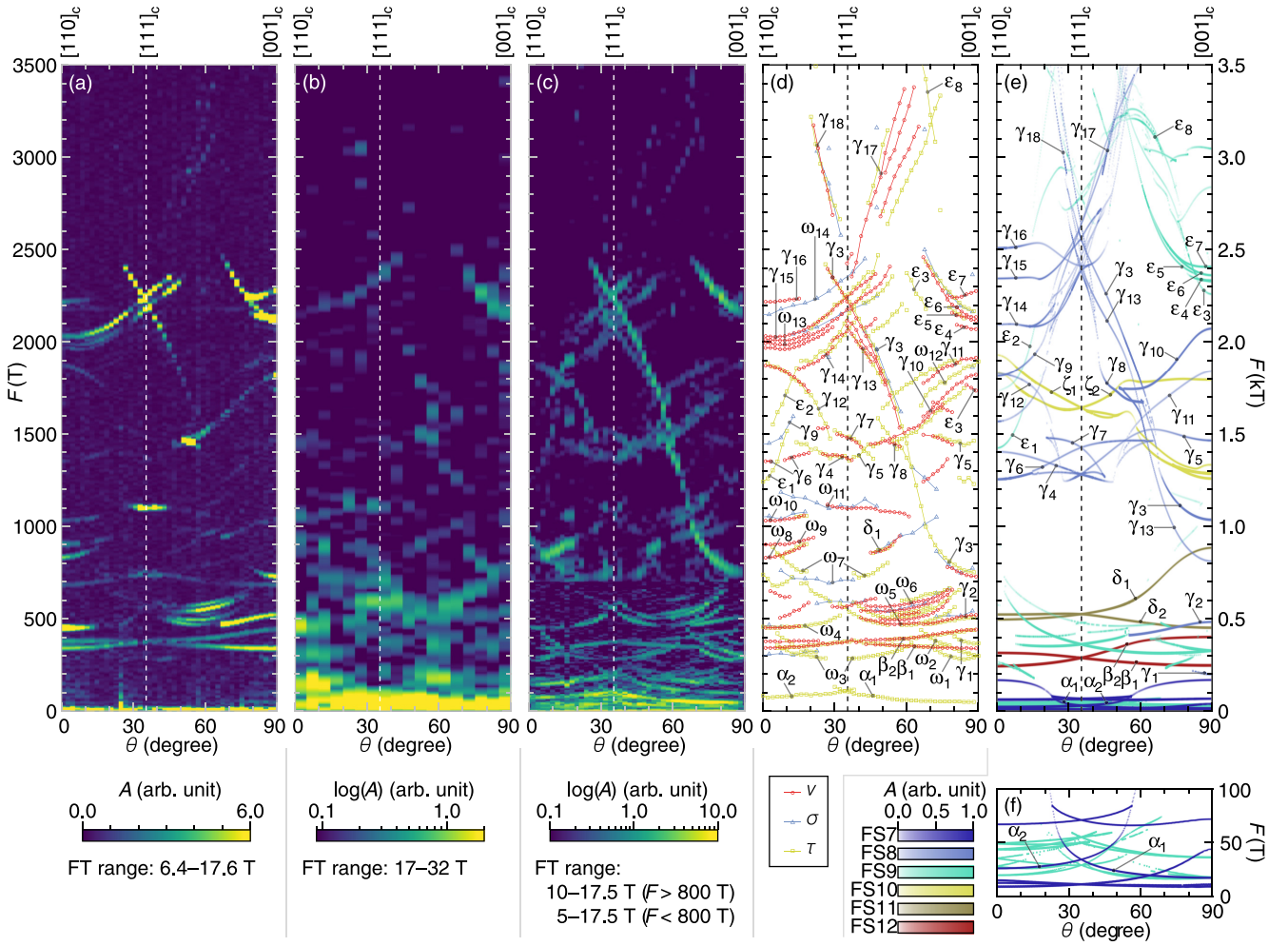


FIG. 4. (a) Angular dependence of Fourier-transformed spectra measured on the AC magnetic susceptibility, (b) electrical conductivity, and (c) magnetic torque [37]. The color scales shown at the bottom indicate the relationship between the color and amplitude A . (d) Angular dependence of the observed frequencies. Higher harmonics are omitted. The lines connecting markers are guides for the eye that are speculated from the angular variation of frequencies and amplitudes. (e) Angular dependence of Fourier-transformed spectra simulated based on the calculated electronic states of phase III. Eq. (1) with $f_q = B^{1/2}/m^*$, $T_D = 0.1$ K, and $T = 50$ mK was used in the simulation, and the field range of 5–17.5 T was used for the Fourier transformation. Higher harmonics are neglected. Colors indicate the corresponding FSs for each branch, and the deeper color corresponds to a larger A , as shown in the color scales at the bottom. The branches corresponding to the experimentally observed branches are labeled. In addition, the δ_2 , ζ_1 , and ζ_2 branches are labeled for explanation. (f) Enlarged view of (e) for $0 \leq F \leq 100$ T.

The δ_1 branch observed for $\theta = 44\text{--}72.5^\circ$ is ascribed to FS11. The simulation for FS11 shows that the amplitude of the oscillations increases significantly around $\theta = 44\text{--}72.5^\circ$ (the more specific simulations in Appendix B show this feature more clearly), which is because of S'' being as small as -0.3 .

The angular dependence of the frequencies and the intensities of the ϵ_{1-8} are close to the simulation for the FS9. Notably, multiple branches ϵ_{3-7} observed near $\theta = 90^\circ$ diverge rapidly as θ decreases; such splitting and divergence of the branches reflect that the FS9 has the additional part that is developing outwards. These features do not emerge from the nearly spherical shape of the FS9 calculated in Ref. [37]. The satisfactory agreement between the experimental and simulated branches described above guarantees that our calculation reproduces most of the real shapes of FSs more closely than those of Ref. [37].

4. Unidentified branches

Nonetheless, there are still some other branches, ω_{1-14} , whose origins remain uncertain. We can speculate their origins to some extent. The ω_{1-4} and ω_{7-11} branches may originate from the crownlike part of the FS9 because we were unable to observe any of the simulated branches arising from the crownlike part that are expected below 800 T [compare Figs. 4(d) and 4(e)]. Perhaps, the crownlike part has a slightly different shape. As seen in its complex shape, the crownlike part comprises an intersection of several bands, which is sensitive to small perturbations; therefore, reproducing the shape, including the fine details, is difficult.

For the ω_5 and ω_6 branches, we observed three branches between them, which are significantly reminiscent of the magnetic breakdown [39,51,52]. The central angle of this fivefold split structure is approximately 60° , which is close to the direction in which the crownlike part develops. Thus, we

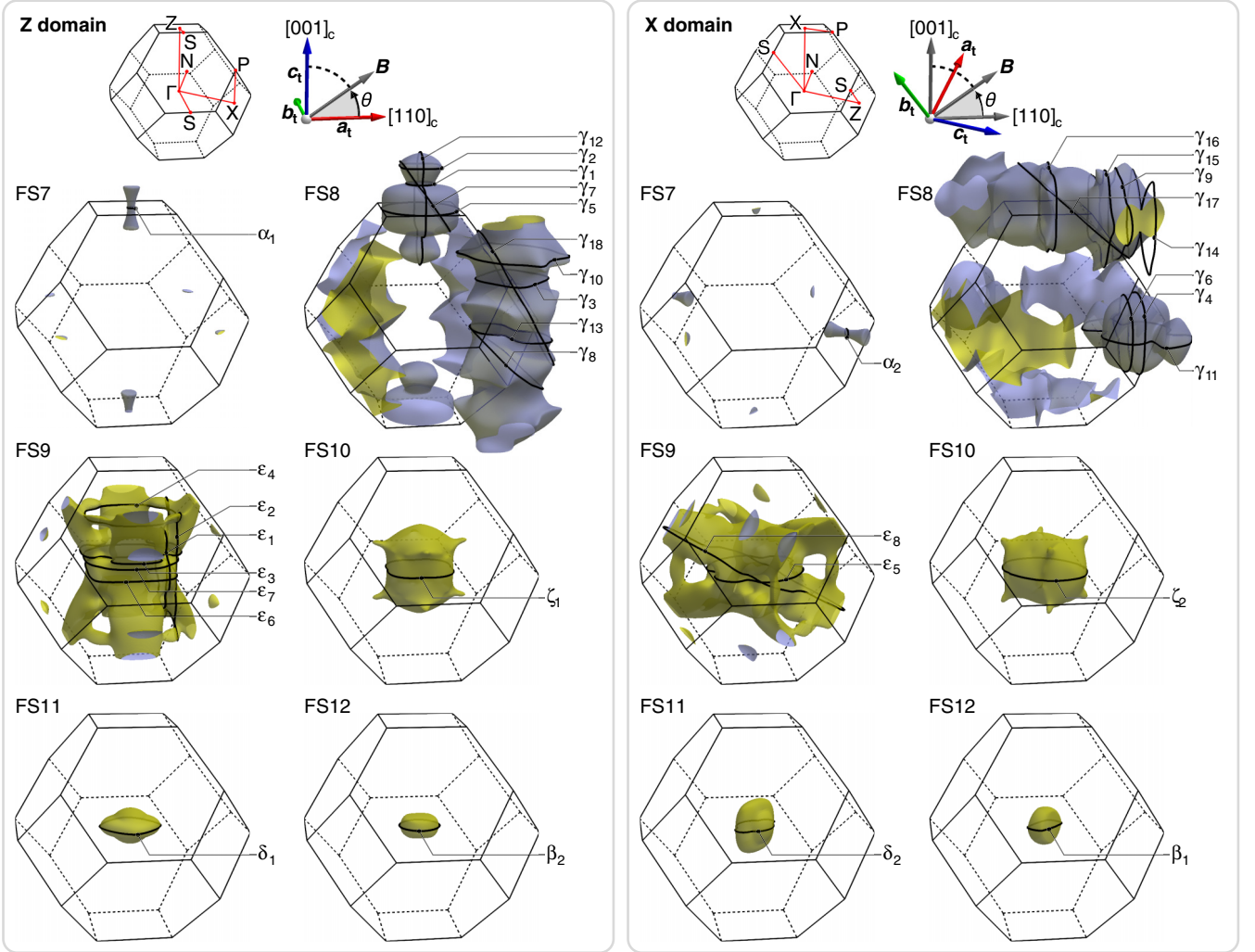


FIG. 5. FSs of $\text{Cd}_2\text{Re}_2\text{O}_7$ calculated for phase III. Extremal orbits corresponding to the observed branches and some major non-observed branches are indicated for the Z (left) and X (right) domains. Purple and yellow surfaces enclose holes and electrons, respectively. The Brillouin zone in phase III is indicated for each domain.

speculate that the ω_5 and ω_6 branches arise from the magnetic breakdown between FS9 and FS8 or between FS9 and FS10.

The ω_{12} branch might be ascribed to a splitting of γ_{11} caused by the misalignment of the crystal, which lifts the degeneracy of the branches arising from the X and Y domains. Similarly, the ω_{14} branch may be ascribed to the splitting of γ_{15} caused by misalignment of the crystal.

However, the ω_{13} branch cannot be explained by a similar splitting of the γ_{15} branch because more splitting of up to four branches (just above and below ω_{13}) was observed around the γ_{15} branch in the modulation method [see Figs. 4(a) and 4(d)]. Recalling that the orthorhombic distortion to $F222$ splits the X and Y domains into two different domains for each, the fourfold splitting of the γ_{15} branch is possibly a hallmark of the symmetry reduction to $F222$ (see Appendix C for a discussion of the symmetry at the lowest temperature).

5. Nonobserved branches

We briefly mention the simulated branches, ζ_1 and ζ_2 , expected from FS10 that were not experimentally observed. We

did not observe any frequency from FS10, which is in contrast with the fact that we observed almost all branches expected from FS8. The absence of FS10 is unlikely in the viewpoint of the carrier compensation between the electrons and holes. The m^* and S'' values simulated for the ζ_1 and ζ_2 branches were small; particularly, m^* and S'' calculated for the ζ_1 branch in $B \parallel \langle 001 \rangle$ were 0.780 and 0.446, respectively, both of which are smaller than those of any branches belonging to FS8 (see Table I). Therefore, the absence of frequencies from FS10 might indicate that the effective masses of the orbits on FS10 are more enhanced than those on FS8. Appendix D describes the m^*/m_b distribution on each FS orbit, where m_b is the bare band mass.

B. Electronic states

1. Optimized crystal structure

The agreement between the experimental and simulated results of the quantum oscillations guarantees the validity of our calculation and enables us to discuss the relationship between the crystal structure and the electronic states of $\text{Cd}_2\text{Re}_2\text{O}_7$.

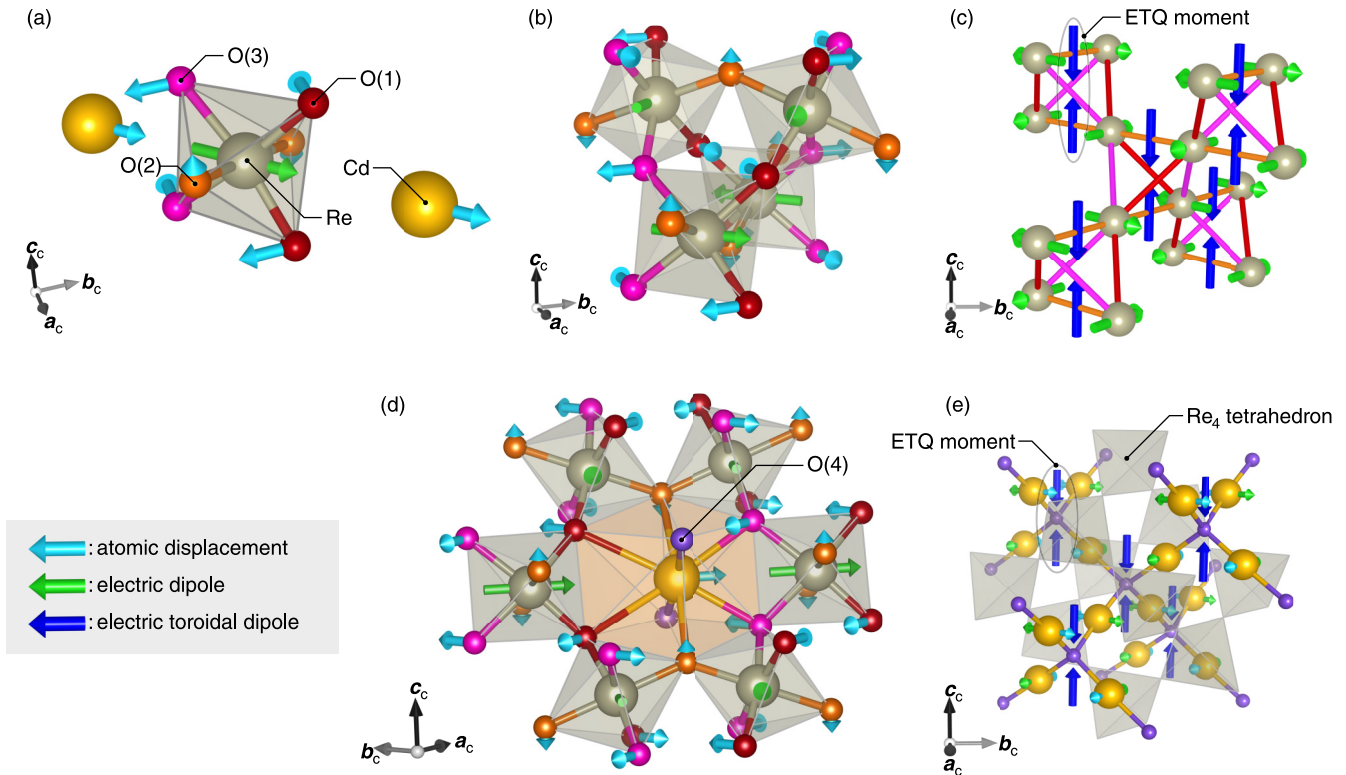


FIG. 6. (a) Atomic displacements (cyan arrows) around a Re atom and (b) Re_4 tetrahedral unit in the optimized crystal structure for phase III. Note that the atomic displacements of Re atoms are antiparallel to the electric dipoles (green arrows), but they are too small to display. (c) Electric dipoles and electric toroidal dipoles (blue arrows) associated with the potential gradient around the Re atom are depicted on a Re pyrochlore lattice. (d) Coordination environment around the CdO_8 dodecahedron. (e) Electric dipoles and electric toroidal dipoles associated with the Cd displacements are depicted on a Cd-O(4) zincblende network interpenetrating a Re pyrochlore lattice. Note that the electric dipoles are antiparallel to the Cd displacements.

First, we compare the optimized structure of phase I with the experimental data. There are two variable parameters in the structure of phase I: the lattice constant a and the atomic coordinate x of the $\text{O}(2_1)$ site (x , $1/8$, $1/8$) [see Fig. 1(a)] [53]. The optimized a is 10.2382 \AA , which is slightly larger than the reported values $10.225\text{--}10.226 \text{ \AA}$ taken at room temperature [14,38,54,55], and almost consistent with 10.2358 \AA taken at 250 K [55]. Thus, the calculated lattice constant reproduces the experimental values within a typical error of the order of 1%. The optimized x is 0.3172 , which agrees well with the experimental values in the range of $0.315\text{--}0.319$ [14,38,54,55]. Therefore, our optimized structure of phase I is consistent with the experiments; thus, that of phase III may also be reliable.

Next, we examine the optimized structure of phase III. Figure 6(a) shows the optimized structure of the ReO_6 units of phase III. The cyan arrows indicate the direction and relative magnitude of the atomic displacements with respect to phase I. The $\text{O}(1_1)$ site surrounding a Re atom splits into three different sites: O(1), O(2), and O(3) (the absence of the “1” subscript of site numbers of oxygen indicates the notation for phase III). Table II lists the atomic coordinates of the optimized structure of phase III, together with the experimental results obtained at 4 K using neutron diffraction [50] and at 90 K using x-ray diffraction [38]. For reference, the displacements from the nondistorted coordinates in phase I are also listed. The atomic

displacements in the optimized structure except for Re are larger than the measured displacements. The difference of the Re displacement between the calculation and experimental results may not be important because the displacement is quite small. The direction of the O(2) displacement in the calculation and experiments are opposite. This may be explained by the electrostatic repulsion between O(2) and O(1); in the calculation, O(2) is repelled from O(1) because the displacement of O(1) is larger than that in the experiments.

The structural parameters may have temperature dependences because the displacements at 4 K are larger than those at 90 K . This is plausible because the order parameters are coupled with the structure and become smaller at higher temperatures. Indeed, physical properties show temperature dependences in phase III [19,20,24,56]. As a continuous and drastic change in magnetic torque is observed below 20 K [33], the electronic states and the structural parameters may drastically change at lower temperatures; this is in stark contrast to ordinary structural transition, in which significant structural change occurs only near the transition temperature and ceases at low temperatures. Note that our calculation corresponds to the limit of absolute zero temperature. Although the optimized structural parameters do not always agree with the experiments, the difference between the optimized structure and the measured one obtained at 4 K may reflect the evolution of the electronic states even below 4 K .

TABLE II. Comparison of the optimized atomic coordinates of phase III with the reported experimental results at 4 K [50] and 90 K [38]. The upper half shows the atomic coordinates x , y , and z . The lower half shows the displacements from the nondistorted coordinates (the optimized structure of phase I) δx , δy , and δz .

		Optimized ^a			4 K ^b			90 K ^c		
		x	y	z	x	y	z	x	y	z
Cd	8 <i>f</i>	0.51311	1/4	1/8	0.51036	1/4	1/8	0.5041(6)	1/4	1/8
Re	8 <i>f</i>	0.99838	1/4	1/8	0.99911	1/4	1/8	0.9967(3)	1/4	1/8
O(1)	8 <i>d</i>	0.17407	0.17407	0	0.18517	0.18517	0	0.1880(20)	0.1880(20)	0
O(2)	8 <i>c</i>	0	0	0.19412	0	0	0.18747	0	0	0.1896(14)
O(3)	8 <i>e</i>	0.20635	0.79365	0	0.20572	0.79428	0	0.1970(20)	0.8030(20)	0
O(4)	4 <i>b</i>	0	0	1/2	0	0	1/2	0	0	1/2
		δx	δy	δz	δx	δy	δz	δx	δy	δz
Cd	8 <i>f</i>	+0.01311	0	0	+0.01036	0	0	+0.0041(6)	0	0
Re	8 <i>f</i>	-0.00162	0	0	-0.00089	0	0	-0.0033(3)	0	0
O(1)	8 <i>d</i>	-0.01809	-0.01809	0	-0.00699	-0.00699	0	-0.0042(20)	-0.0042(20)	0
O(2)	8 <i>c</i>	0	0	+0.00196	0	0	-0.00469	0	0	-0.0026(14)
O(3)	8 <i>e</i>	+0.01419	-0.01419	0	+0.01356	-0.01356	0	+0.0048(20)	-0.0048(20)	0
O(4)	4 <i>b</i>	0	0	0	0	0	0	0	0	0

^aCell parameters are fixed to $a = a_c/\sqrt{2}$, $c = a_c$, where a_c is the optimized lattice constant in phase I (10.2382 Å).

^bData were measured using neutron diffraction. The cell parameters are $a = 7.239$ Å, $c = 10.242$ Å. As the reported coordinates are in the opposite chirality relative to ours, we reversed the chirality of their data.

^cData were measured using x-ray diffraction. The cell parameters are $a = 7.2313(4)$ Å, $c = 10.2282(6)$ Å.

2. Changes in the band structures

The calculated band structures for phases I and III are shown in Figs. 7(a) and 7(b), respectively. Because phases I and III have the same sizes of the Brillouin zone, for clarity, we used the high-symmetry k -point notation of phase III for phase I, as indicated in Fig. 5. We also used the same vacuum levels in the calculations for phases I and III; therefore, the small difference in E_F is essential. We define the zero of energy as the E_F in phase III. The band structure of phase I is almost consistent with those of previous reports [57,58]: The E_F lies on the Re t_{2g} bands. The spherical hole pocket lies around the S point, whereas two electron pockets are nested around the Γ point.

In the band structure for phase III, the number of band lines is doubled because of the SOI-induced spin splitting asso-

ciated with inversion symmetry breaking. Besides, the band width becomes broader, and E_F is increased by 89 meV. The calculated carrier number of electrons or holes in phase III is $8.7 \times 10^{20} \text{ cm}^{-3}$, which almost agrees with $8.0 \times 10^{20} \text{ cm}^{-3}$ determined by the Hall effect [19].

3. Density-of-states broadening

The difference of the electronic states between phases I and III is more apparent in the calculated DOS shown in Fig. 7(c). In phase I, E_F lies on a shoulder of peak. The DOS at E_F is $14.60 \text{ states eV}^{-1}$ and per formula unit (f.u.) (spin degeneracy is included), which is dominated by heavy hole bands possessing twelvefold degeneracy due to the six Γ -Z(X) lines. In phase III, the peak is broadened due to structural distortion. Therefore, the E_F increases, and the DOS at E_F decreases to

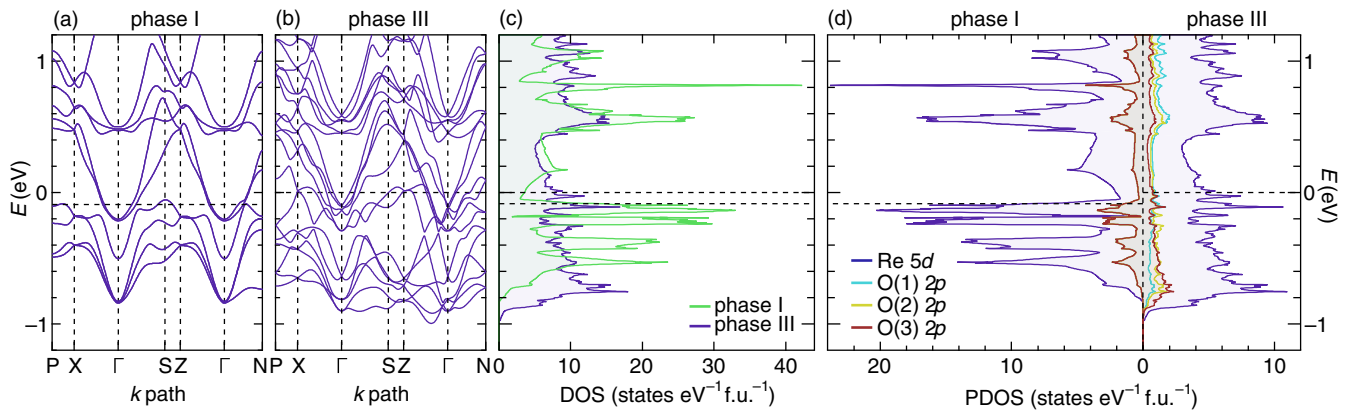


FIG. 7. (a) Calculated band dispersions for phase I and (b) phase III. The E_F 's are indicated as horizontal dashed lines. For phase I, the same k -point notations with phase III are used. (c) Total DOS for phases I and III. (d) PDOS of the Re 5*d*, O(1) 2*p*, O(2) 2*p*, and O(3) 2*p* states in phase III (right), and the corresponding states in phase I (left). Note that the PDOS corresponding to the O(1) 2*p*, O(2) 2*p*, and O(3) 2*p* states in phase I are equivalent to the O(1₁) 2*p* states.

TABLE III. Bond angles and lengths in the optimized crystal structures of phases I and III.

	Angle		Length (\AA) ^a
Phase I			
$\angle \text{Re-O}(1_1)\text{-Re}^b$	138.39°	$\text{Re-O}(1_1)^b$	1.9361
Phase III			
$\angle \text{Re-O}(1)\text{-Re}$	148.59°	$\text{Re-O}(1)$	1.8867
$\angle \text{Re-O}(2)\text{-Re}$	137.29°	$\text{Re-O}(2)$	1.9433
$\angle \text{Re-O}(3)\text{-Re}$	130.87°	$\text{Re-O}(3)$	1.9836

^aCell parameters in phase III are fixed to $a = a_c/\sqrt{2}$, $c = a_c$, where a_c is the optimized lattice constant in phase I (10.2382 \AA).

^bO(1), O(2), and O(3) sites in phase III are equivalent to O(1₁) site in phase I.

7.68 states $\text{eV}^{-1} \text{f.u.}^{-1}$, which corresponds to the bare band specific heat coefficient $\gamma_b = 9.05 \text{ mJ mol}^{-1} \text{K}^{-2}$. Compared with the measured value of $\gamma = 30.15 \text{ mJ mol}^{-1} \text{K}^{-2}$ [12], we obtain a total mass enhancement factor of $\langle m^*/m_b \rangle = \gamma/\gamma_b = 3.33$ at the lowest temperature. The decrease in the DOS at E_F from phases I to III is approximately 50%, which agrees well with the experimental estimation [17,19].

Notably, the DOS broadening results in an increase in the DOS in the lower energy region (-0.6 to -1.0 eV), which significantly contributes to the stabilization of phase III relative to phase I. The corresponding changes in the Re-O bonding state can be seen in the optimized crystal structure [see Fig. 6(b)]. The bond angles and lengths in the optimized structures are summarized in Table III. The Re-O(1)-Re angle rises from 138.39° in phase I to 148.59° in phase III. Generally, the increase in the $B\text{-O}(1_1)\text{-B}$ angle in pyrochlore oxide $A_2B_2O(1_1)_6O(2_1)$ enhances the overlap between the $B t_{2g}$ and $O(1_1) 2p$ orbitals [59,60]; thus, the orbital overlap of the Re-O(1) bond is enhanced in phase III. In contrast, the Re-O(3)-Re angle decreases to 130.87° in phase III, which diminishes the orbital overlap. In terms of bond length, the Re-O(1) becomes shorter, whereas the Re-O(3) becomes longer in phase III, both of which are consistent with the enhancement and reduction of the orbital overlap, respectively. As the enhancement (reduction) of the orbital overlap generally results in (de)stabilization, the changes in the Re-O bonding states broaden the DOS.

However, DOS broadening has another aspect. To see the details of DOS broadening, we calculated the projected DOS (PDOS) of the Re $5d$, O(1) $2p$, O(2) $2p$, and O(3) $2p$ states in phase III and the corresponding states in phase I, as shown in Fig. 7(d). The states near E_F are primarily composed of Re $5d$ states and a small amount of O(1–3) $2p$ states, as expected, whereas the contributions from the other states, such as Cd $4d$, are negligibly small (not shown). In phase III, the contributions of the O(1), O(2), and O(3) states vary in energy: Among the O $2p$ states, the O(3) $2p$ states are dominant in the occupied low-energy states, whereas the O(1) $2p$ states are dominant in the unoccupied high-energy states. This indicates that the O(3) $2p$ states are stabilized, whereas the O(1) $2p$ states are destabilized in phase III. This appears to be inconsistent with the changes in the Re-O bonds in the crystal structure.

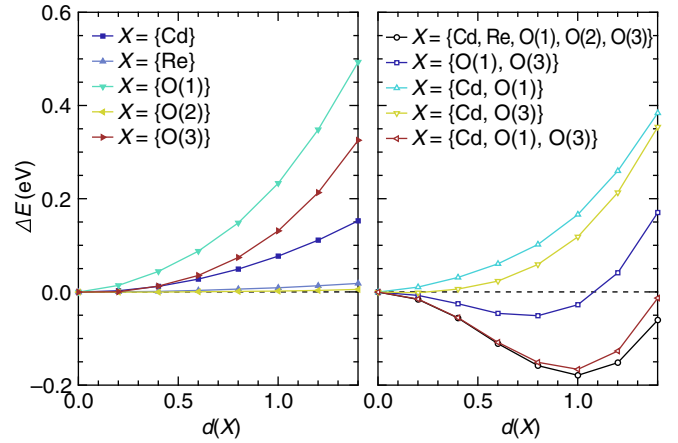


FIG. 8. Total energy change ΔE as a function of the normalized atomic displacement magnitude $d(X)$ for the selected crystallographic sites X . Here, X is a subset of the crystallographic sites in phase III: {Cd, Re, O(1), O(2), O(3)}. In a structure corresponding to $d(X)$, only the selected sites X are displaced, from the optimized structure of phase I. The magnitude of displacements is multiplied by $d(X)$ relative to those in the optimized structure of phase III. The displacements in the other sites are fixed to zero.

This counterintuitive consequence stems from the electrostatic potential associated with the Cd ion. As shown in Figs. 6(a) and 6(d), the O(3) displacement is in the direction approaching the Cd, whereas the O(1) displacement is in the direction away from the Cd. In addition, the Cd itself is displaced toward the O(3). Because the Cd ion is positively charged, the closer to the Cd, the lower the energy of the negatively charged O ions and *vice versa*. Thus, the changes in the O(1) $2p$ and O(3) $2p$ states in PDOS reflect the changes in the atomic levels. It seems that the changes in both the Re-O bonding states and the atomic levels of O $2p$ states are involved in DOS broadening.

4. Essential atomic displacements on energy gain

To analyze the factors that contribute to the energy stabilization in phase III, we examined the contribution of the atomic displacement of each site. We calculated the evolution of energy starting from phase I along with displacements of the selected crystallographic sites. Figure 8 shows the energy difference (ΔE) as a function of the normalized displacement magnitude [$d(X)$]. Here, X is a subset of crystallographic sites in phase III, {Cd, Re, O(1), O(2), O(3)}. In a structure corresponding to $d(X)$, only the selected sites X are displaced with a magnitude multiplied by $d(X)$ which is relative to those in the optimized structure of phase III, with the displacements of other sites fixed to zero; i.e., $d(X) = 0$ corresponds to the structure of phase I and $d(X) = 0.4$ with $X = \{\text{O}(1), \text{O}(3)\}$ corresponds to a structure in which only O(1) and O(3) are displaced by a factor of 0.4.

First, the contributions of Re and O(2) to the energy change are small because their magnitudes of displacement are tiny. Next, the displacement of any single crystallographic site does not achieve any energetic benefit. This can be interpreted as follows: Even if only the O(3) approaches the Cd and gains

electrostatic stabilization, destabilization caused by the elongated Re-O(3) bond may be even larger.

Subsequently, considering the combination of displacements, we find that the subset $X = \{O(1), O(3)\}$ produces an energy gain, whereas $X = \{Cd, O(1)\}$ and $X = \{Cd, O(3)\}$ do not. This indicates that the combination of the O(1) and O(3) displacements plays an essential role in the stability of phase III. These displacements result in shortened Re-O(1) and elongated Re-O(3) bonds, which is the bond-ordered state corresponding to the $3z^2 - r^2$ -type ETQ order proposed in Ref. [6].

Finally, adding Cd displacement here provides an energy stabilization to the same extent as when all sites are displaced. Notably, the additional Cd displacement significantly enhances the energetic benefit and increases the magnitude of displacements at the minimum energy compared with the case of $X = \{O(1), O(3)\}$. It seems that the Cd displacement enhances the Re-O bond order by electrostatically attracting O(3), reducing the electrostatic repulsion between O(3) and O(1) and then allowing the even shorter Re-O(1) bond. In this sense, the Cd displacement can be interpreted as an assistive process of the bond-ordered state to produce additional stabilization.

5. ETQ order in the crystal structure

It is instructive to visualize the ETQ moments in the optimized crystal structure appearing because of the bond-ordered state. For this purpose, we depicted the charge density difference between phases I and III within the plane containing the Re, O(1), and O(3) sites in Fig. 9(a) [see the three-dimensional coordination environment around the Re site shown in Fig. 6(a)]. The O(3) and Cd displacements cause a relative increase in the charge density within the region surrounded by the Cd and O(3) sites. In addition, at the opposite location of the Re, the O(1) and Cd displacements cause a relative decrease in charge density. Therefore, there is a charge density gradient around the Re site.

Although $Cd_2Re_2O_7$ is metal, this local “electric dipole” is not screened by conduction electrons. This is because the scale of the Thomas-Fermi screening is the order of an inverse of the Fermi wave number $\sim k_F^{-1}$ [61], which is comparable to several angstroms [62]. Hence, a local potential gradient exists around Re, as shown in Fig. 9(b). Thus, Re $5d$ electrons experience a large antisymmetric SOI (ASOI), as demonstrated by the giant spin splitting in the hole FSs.

The directions of the electric dipoles at the Re sites are represented in Fig. 6. The electric dipoles in a Re_4 tetrahedral unit form two opposing uniaxial electric toroidal dipole moments, which is equivalent to a $3z^2 - r^2$ -type ETQ moment in total [see Fig. 2 and the notation in Fig. 6(c)]. In the entire Re pyrochlore network, the ETQ moments align in the same orientation on each Re_4 tetrahedral unit. Note that in the opposite chirality domain, the direction of the ETQ moment is the opposite. Because this ETQ order occurs in the metallic state, we will call this the metallic ETQ order.

It is worth pointing out that we can find another ETQ moment in the Cd-O(4) zincblende network by considering the displacement of the Cd as an electric dipole, as depicted in Fig. 6(e). This is because Re and Cd are located at the

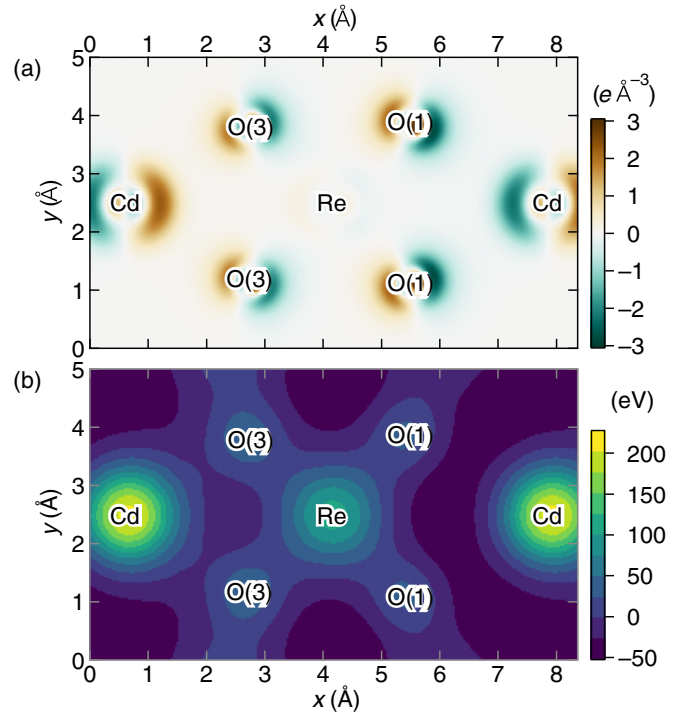


FIG. 9. (a) Charge density difference between structures of phases I and III through the plane containing the O(1) and O(3) sites with $d(X) = 0$, surrounding a Re. [For $d(X) \neq 0$, they are not exactly on the same plane.] Note that the charge density drops around the core owing to the use of pseudopotentials. (b) Total potential map calculated for the optimized crystal structure for phase III in the same plane as in (a). The interval of contour levels is 25 eV.

same Wyckoff position $8f$. Interestingly, the sign of the ETQ moment is the same as the former one in the Re_4 tetrahedra. However, the former is more essential than the latter because the Re $5d$ electrons dominate the electronic states near the E_F .

We would like to emphasize that the metallic ETQ order found in the optimized crystal structure (in real space) and spin-split FSs shown in Fig. 5 (in momentum space) correspond to each other through our calculation. Thus, the agreement of the FSs between the experiments and the calculation provides indirect evidence of the metallic ETQ order. Therefore, our results provide a microscopic picture of the order in the real and momentum spaces of $Cd_2Re_2O_7$ at the lowest temperature.

IV. DISCUSSION

A. Electron-phonon and electron-electron interactions

The mass enhancement, compared with the electronic structure calculation using the conventional DFT method, is caused by the many-body interactions not included in the calculation. It is empirically known that even the DFT + U calculation hardly includes the mass enhancement [63]. Thus, we can approximately evaluate the mass enhancement factor by comparing the experimentally obtained m^* with m_b calculated by DFT + U method. The $\langle m^*/m_b \rangle$ represents the FS-averaged enhancement factor, which can be expressed as

$$\langle m^*/m_b \rangle = (1 + \lambda_{ep})(1 + \lambda_{ee}), \quad (2)$$

where the λ_{ep} and λ_{ee} are the electron-phonon and electron-electron coupling parameters, respectively.

The strengths of the electron-phonon and electron-electron interactions in $\text{Cd}_2\text{Re}_2\text{O}_7$ have been controversial. The low-temperature coefficient of the T^2 term (A) in electrical resistivity is one of the indicators of the electron-electron interaction as it reflects the electron-electron scattering. The value of A was evaluated as $9(4) \times 10^{-3} \mu\Omega \text{ cm K}^{-2}$ [12] after subtracting the Koshino-Taylor contribution due to the nonmagnetic impurity scattering [64,65]. The Kadowaki-Woods ratio $R_{\text{KW}} = A/\gamma^2$ using A is $10(5) \mu\Omega \text{ cm mol}^2 \text{ K}^2 \text{ J}^{-2}$, which is comparable to the universal value $\sim 10 \mu\Omega \text{ cm mol}^2 \text{ K}^2 \text{ J}^{-2}$ [66] for the heavy fermion system, even though $\langle m^*/m_b \rangle$ of $\text{Cd}_2\text{Re}_2\text{O}_7$ is considerably smaller than those observed in heavy fermion materials (100–1000). Thus, the electron-electron interaction in $\text{Cd}_2\text{Re}_2\text{O}_7$ is presumably strong.

For the electron-phonon coupling, all experiments on the superconducting properties provide evidences of the weak-coupling nature: The superconducting gap $\Delta(0)$ and the magnitude of the specific heat jump ΔC_e at T_c were evaluated as $\Delta(0)/k_B T_c = 1.84\text{--}2.5$ [17,31,67,68] and $\Delta C_e/\gamma T_c = 1.15\text{--}1.29$ [30,31], respectively, both of which are comparable to the weak-coupling Bardeen-Cooper-Schrieffer (BCS) values (1.76 and 1.43, respectively). Therefore, the electron-phonon coupling should be small.

In contrast, the small spin magnetic susceptibility $\chi_s = 1.38 \times 10^{-4} \text{ cm}^3 \text{ mol}^{-1}$ and large γ yield an anomalously small Wilson ratio $R_W = 0.34$ [17,19], which is generally unity for free electrons and two for strongly correlated electrons [69]. Such a small value of R_W typically indicate that the electron-electron coupling is small and/or the strong electron-phonon coupling mostly enhances γ but not χ_s .

To overcome these discrepancies, we evaluated the λ_{ep} and λ_{ee} to facilitate the quantitative discussion. With the assumption of a phonon-mediated BCS superconductivity in $\text{Cd}_2\text{Re}_2\text{O}_7$, the McMillan equation [70] yields the λ_{ep} as

$$\lambda_{\text{ep}} = \frac{\mu^* \ln(1.45T_c/\Theta_D) - 1.04}{(1 - 0.62\mu^*) \ln(1.45T_c/\Theta_D) + 1.04} \quad (3)$$

for $\mu^* \leq \lambda_{\text{ep}} \leq 1.5$, where Θ_D is the Debye temperature measured as 458 K [31], and μ^* is the Coulomb pseudopotential parameter. Using the Benneman and Garland empirical formula [71], μ^* can be estimated as

$$\mu^* = \frac{0.26N(E_F)}{1 + N(E_F)}, \quad (4)$$

where $N(E_F)$ is the DOS at E_F in units of states $\text{eV}^{-1} \text{ atom}^{-1}$. Because $N(E_F) = 0.698$ from our calculation, μ^* is calculated as 0.107, which is slightly lower than the standard value of 0.13. Therefore, λ_{ep} is obtained from Eq. (3) as 0.380. This value is consistent with the weak-coupling scenario. Subsequently, using $\langle m^*/m_b \rangle$ and λ_{ep} values, we obtain $\lambda_{\text{ee}} = 1.41$; this indicates that m^* is mainly enhanced by the electron-electron interaction, as expected from the R_{KW} . The large λ_{ee} is in line with the fact that we need $U = 4.5 \text{ eV}$ to reproduce the observed FSs in our calculation. By comparing the λ_{ep} , λ_{ee} , and R_W values with related compounds, it is clear that a small R_W value does not necessarily indicate a small electron-electron interaction and/or a large electron-phonon

interaction and that there is a hidden factor making R_W small (see Appendix E).

B. Driving force of the metallic ETQ order

In the early study, the mechanism of the phase transition from phase I to the noncentrosymmetric phases was speculated as being similar to a band Jahn-Teller effect [19], where the energy of the occupied (unoccupied) band decreases (increases) owing to symmetry reduction. Indeed, according to our study, half of the spin-split hole FS (FS7) almost disappears, and the other part of the spin-split hole FS (FS8) becomes significantly large in phase III (see Fig. 5); this situation is similar to the spin-split version of the band Jahn-Teller effect associated with an inversion-symmetry breaking. In addition, in terms of the DOS, the band Jahn-Teller effect is characterized by large DOS in a high symmetry phase [21], which is also the case with $\text{Cd}_2\text{Re}_2\text{O}_7$ where E_F lies on the shoulder of the DOS peak in phase I [see Fig. 7(c)]. However, our calculation revealed that this is only partially true and is not likely the total picture of the phase transition. This is because E_F rises from phase I to III owing to DOS broadening; therefore, the energy gain by spin splitting near E_F is limited.

Another mechanism recently theoretically proposed in Ref. [3] is the odd-parity electronic nematic state driven by Pomeranchuk-type Fermi-liquid instability in the p -wave spin interaction channel. This instability arises when metals with inversion symmetry have both a strong SOI and electron-electron interaction. Indeed, we confirmed the large spin splitting of the FSs owing to the strong SOI and obtained a λ_{ee} of 1.41, which highlights the strong electron-electron interaction. The theory predicts the formation of the odd-parity multipolar order as a consequence of a Fermi-liquid instability, which is consistent with the metallic ETQ order in our optimized crystal structure. Importantly, the bond order of Re-O(1) and Re-O(3) associated with the metallic ETQ order plays an essential role in the energy stabilization in phase III. In this respect, it is plausible that the metallic ETQ order in phase III is driven by a Fermi-liquid instability.

V. CONCLUSION

We studied the electronic states of $\text{Cd}_2\text{Re}_2\text{O}_7$ at the lowest temperature by combining quantum oscillations and electronic structure calculations. Based on the optimized crystal structure obtained by the DFT + U calculation with the symmetry constrained to the $I4_122$ space group, we successfully obtained the electronic states that satisfactorily reproduced complex spectra of the observed quantum oscillations. The determined FSs highlight the giant spin splitting in the hole FSs, demonstrating the strong influence of the ASOI. In addition, we confirmed the strong electronic correlation by evaluating the λ_{ee} as 1.41. In the optimized crystal structure, we visualized the $3z^2 - r^2$ -type metallic ETQ order characterized by the potential gradient around the Re sites owing to the Re-O bond order. Our results demonstrate the microscopic picture of the metallic ETQ order in real and momentum spaces, which is presumably driven by a Fermi-liquid instability associated with the strong SOI and electronic correlation.

As future prospects, we expect the quantitative prediction of the various properties anticipated in the metallic ETQ state

in phase III based on the electronic states obtained in this study. In addition, to observe the off-diagonal responses in experiments, it is inevitable to align not only the tetragonal domains [20] but also the chirality domains observed in Ref. [35]. Thus, a method to produce an energy difference between the opposite chirality domains is required. If one can quantitatively estimate the possible ways to achieve this based on the calculated electronic states, it will significantly promote the realization of experiments. In addition, we expect that the parameters and techniques used in this study will be applied to elucidate the electronic states of phase II and high-pressure phases. Furthermore, in our study, we were unable to clarify how the strengths of the electronic correlation and SOI are involved in determining the ordering manner. Thus, it would be interesting to investigate the hypothetical stable structures by varying these parameters using the technique demonstrated in Ref. [72].

ACKNOWLEDGMENTS

We would like to thank Assoc. Prof. Takumi Hasegawa for his valuable comments. This work was supported by Grants-in-Aid from the MEXT/JSPS of Japan (Grants No. 17H01144, No. JP17H07349, No. 18H04308, and No. 20H01858). A portion of this work was performed at the National High Magnetic Field Laboratory, which is supported by the National Science Foundation Cooperative Agreement No. DMR-1157490 and the State of Florida. We would like to thank Editage (www.editage.com) for English language editing.

APPENDIX A: U AND J DEPENDENCES OF THE OPTIMIZED STRUCTURE AND THEIR ELECTRONIC STATES

Figure 10(a) shows the U dependence of the atomic displacements in the optimized structure of phase III with J fixed to 0.3 eV. Displacements δx or δz of Cd, Re, O(1), O(2), and O(3) are measured from the phase I structure optimized with $U = 4.5$ eV and $J = 0.3$ eV and are plotted against U . The vertical axes are oriented such that the upper part of the graph corresponds to larger displacements. At $U = 0$ eV, the magnitudes of all displacements are considerably larger than the experimental values obtained at 4 K (see Table II). As U increases, the relatively large displacements of Cd, O(1), and O(3) decrease at accelerated rates and approach the experimental values. For atoms with relatively small displacements, the Re displacement exhibits a monotonic increase with increasing U , whereas the O(2) displacement has a minimum at approximately $U = 4$ eV and increases for higher U values.

Corresponding to the optimized structures with various U values, the carrier number of electrons (n_e) or holes (n_h) varies with U . Figure 10(b) shows the n_e ($=n_h$) as a function of U . At $U = 0$ eV, $n_e = 6.0 \times 10^{20} \text{ cm}^{-3}$, which is slightly smaller than the experimental value $8.0 \times 10^{20} \text{ cm}^{-3}$ [19]. As U increases, n_e increases and approaches the experimental value at approximately $U = 4.0$ – 4.5 eV.

Figures 11(b), 11(c), 11(d), and 11(e) show the simulated Fourier-transformed spectra as a function of field direction based on the crystal structures optimized with $U = 0, 4.0, 4.5,$ and 5.0 eV, respectively. A typical $f_q = B^{1/2}/m^*$ is used

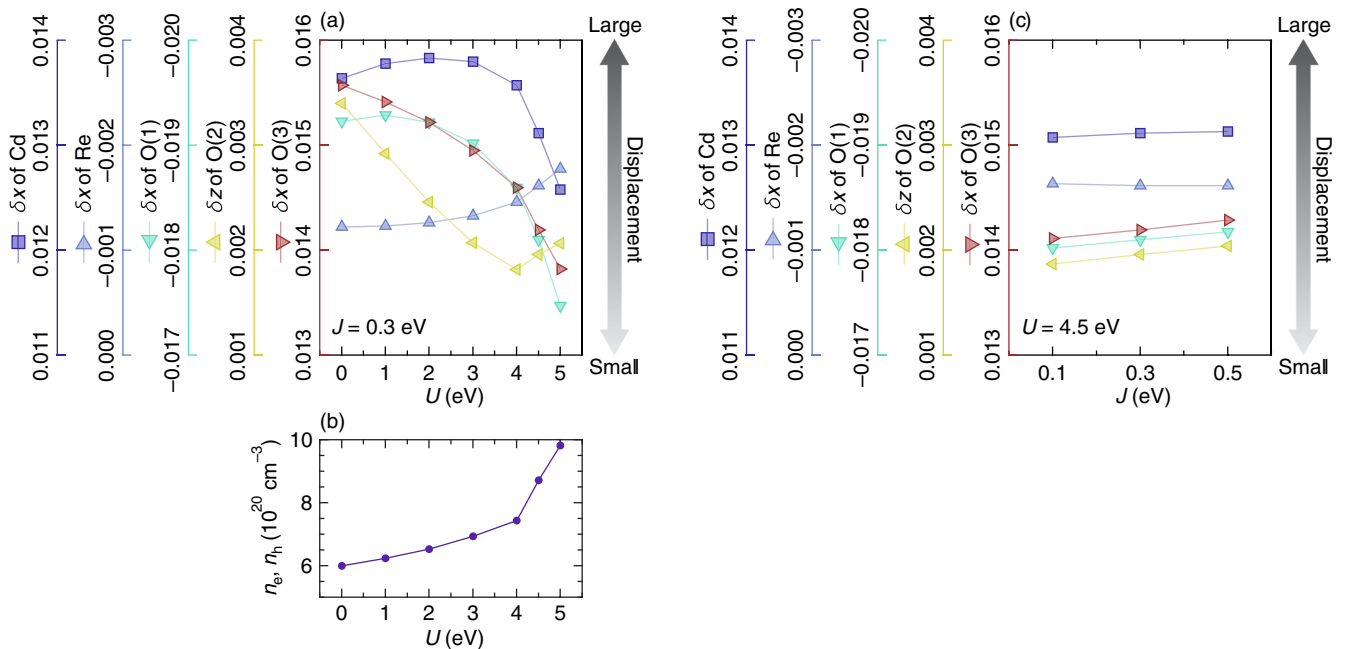


FIG. 10. (a) Atomic displacement coordinates δx or δz for Cd, Re, O(1), O(2), and O(3) in the optimized structure of phase III as a function of the screened Coulomb parameter U used in the optimization procedure. Five left axes represent the vertical axis ranges for each plot. Note that the displacement is larger in the upper part of the graph. The screened exchange parameter J is fixed to 0.3 eV. All displacement coordinates are measured from the optimized phase I structure obtained using $U = 4.5$ eV and $J = 0.3$ eV. (b) Carrier number of electrons (n_e) or holes (n_h) as a function of U . The carrier numbers correspond to the optimized crystal structures in (a). (c) Atomic displacement coordinates δx or δz for Cd, Re, O(1), O(2), and O(3) in the optimized structure of phase III as a function of J used in the optimization procedure. The value of U is fixed to 4.5 eV. The configuration of the vertical axes and the definition of the displacement coordinates are the same as in (a).

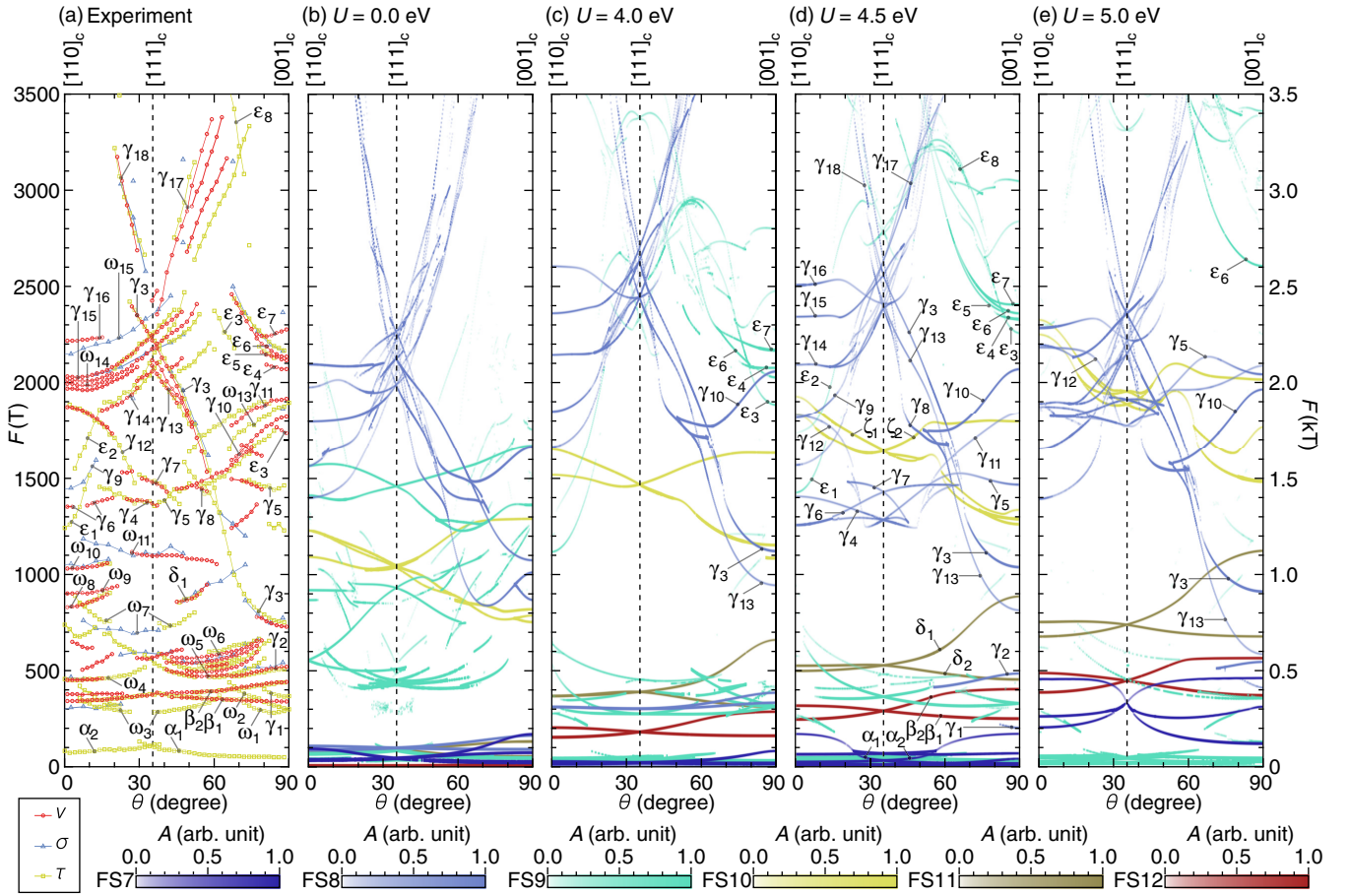


FIG. 11. (a) Angular dependence of the observed frequencies without higher harmonics. This is the same as Fig. 4(d). (b) Angular dependence of the Fourier-transformed spectra simulated based on calculated electronic states optimized with $U = 0.0$ eV, (c) $U = 4.0$ eV, (d) $U = 4.5$ eV, and (e) $U = 5.0$ eV. J is fixed to 0.3 eV. In all calculations, Eq. (1) with $f_q = B^{1/2}/m^*$, $T_D = 0.1$ K, and $T = 50$ mK were used for the simulations of quantum oscillations, and a field range of 5 – 17.5 T was used for the Fourier transformation. Higher harmonics are neglected. The colors indicate the corresponding FSs for each branch, and a deeper color corresponds to a larger amplitude (A), as shown in the color scales at the bottom. (d) is the same as Fig. 4(e).

in the simulation. As indicated by the same color scales as those shown in Fig. 4(e), shown at the bottom, the deeper color corresponds to a larger amplitude, and we used different colors for the branches derived from each FS. Figure 11(a) is the angular dependency of the observed fundamental frequencies shown for the ease of comparison. At $U = 0$ eV, the spectra are completely different from those of the experiments; the sizes of FS11 and FS12 are too small, and the ε_{3-7} branches of FS9 are absent. At $U = 4.0$ eV, the spectra are similar to the experimental results but still have insufficient parts; the γ_1 , γ_2 , γ_{4-7} , γ_{11} , and γ_{12} branches derived from the large hole pocket of FS8 around point Z are completely absent. At $U = 4.5$ eV, we obtained the simulation closest to the experimental results as described in the main text. This U value agrees with the range in which the carrier number coincides with the experiment. At $U = 5.0$ eV, the spectra become different from the experimental results; the ε_6 , γ_5 , and γ_{12} branches become larger than those at $U = 4.5$ eV. Therefore, we conclude that the calculated electronic structure with $U = 4.5$ eV best describes the real electronic structure.

This U value is slightly larger than $U = 3.0$ eV used in a previous study [38]. However, the value used in the previous

study was calculated for impurity states in Rb [73]. In general, U is not transferable from one material to another. For reference, we obtained $U = 4.2$ eV from the calculation based on the phase I structure of $\text{Cd}_2\text{Re}_2\text{O}_7$ and using the linear-response method as implemented in QUANTUM ESPRESSO [74]. This value is consistent with $U = 4.5$ eV determined by the quantum oscillation spectra. Therefore, our conclusion of $U = 4.5$ eV is reasonable from a computational viewpoint.

Next, we present the dependence of the optimized structural parameters and their corresponding electronic states on J with U fixed at 4.5 eV. Figure 10(c) shows the dependence on J of the atomic displacements in the optimized structure of phase III. It is apparent that the variation in the structural parameter is minimal in the range of $J = 0.1$ – 0.5 eV. Figure 12 compares the simulated Fourier-transformed spectra corresponding to the calculation conditions and the structural parameters given in Fig. 10(c). The differences in the quantum oscillation spectra are almost negligible. Therefore, it is difficult to determine a reasonable value of J by comparing the simulated and observed spectra, and thus the use of a typical value of $J = 0.3$ eV does not affect our results.

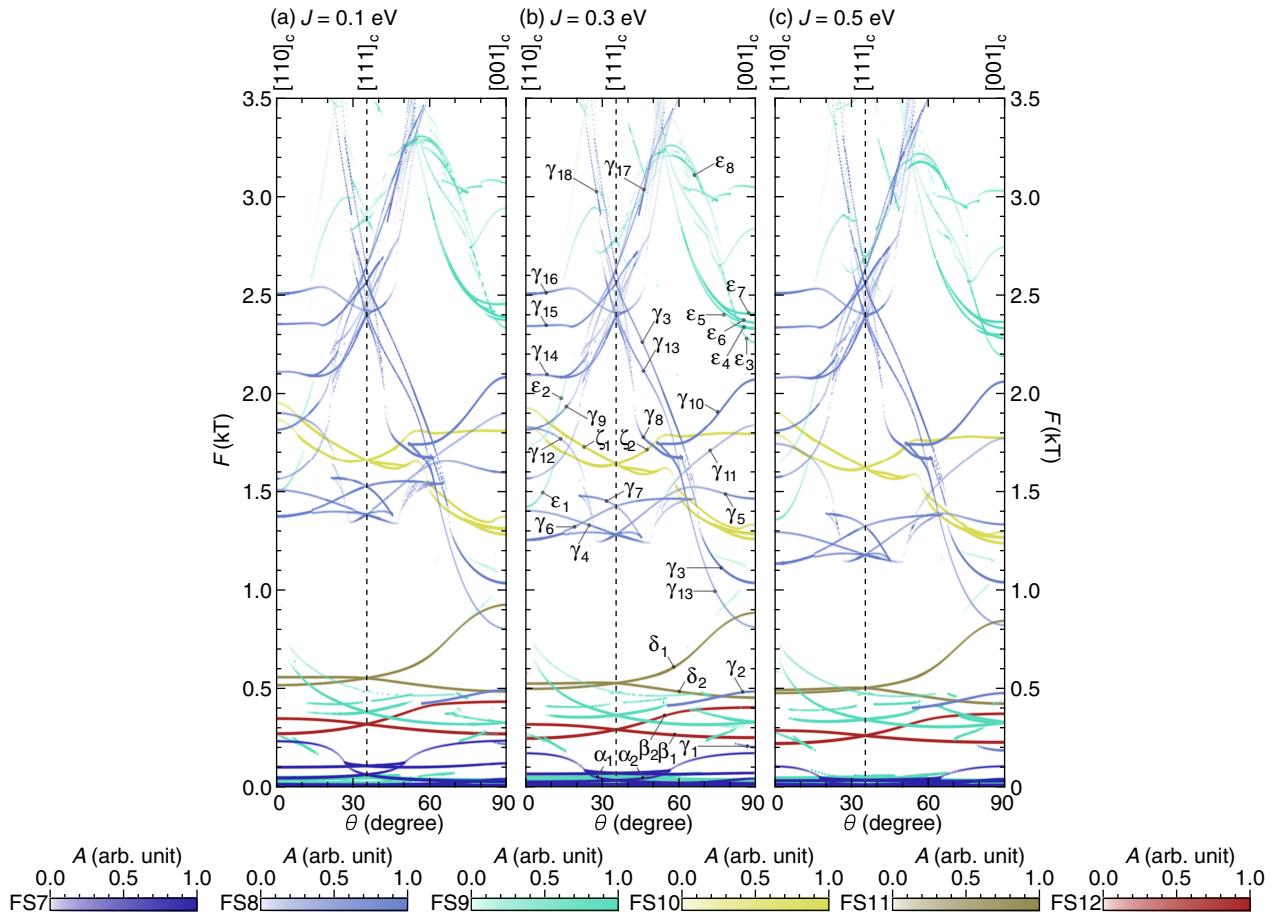


FIG. 12. (a) Angular dependence of the Fourier-transformed spectra simulated on the basis of the calculated electronic states optimized with $J = 0.1$ eV, (b) $J = 0.3$ eV, and (c) $J = 0.5$ eV. U is fixed to 4.5 eV. In all calculations, Eq. (1) with $f_q = B^{1/2}/m^*$, $T_D = 0.1$ K, and $T = 50$ mK were used for the simulations of quantum oscillations, and a field range of 5–17.5 T was used for the Fourier transformation. Higher harmonics are neglected. The colors indicate the corresponding FSs for each branch, and a deeper color corresponds to a larger amplitude (A), as shown in the color scales at the bottom. (b) is the same as in Fig. 4(e).

APPENDIX B: SIMULATED FOURIER-TRANSFORMED SPECTRA

Figures 13(a), 13(b), and 13(c) show the color image of the Fourier transformed spectra as a function of the field direction calculated using f_v , f_σ , and f_τ , respectively.

APPENDIX C: LOW TEMPERATURE SYMMETRY

Most of the observed quantum oscillations can be reproduced well using electronic states calculated based on the $I4_122$ space group. Therefore, the symmetry of the crystal at the lowest temperature seems to be “almost” $I4_122$. However, a fourfold split structure was observed around the γ_{15} branches, suggesting the possibility that the X and Y domains of the $I4_122$ phase may split into four types because of the tiny orthorhombic distortion. Actually, there are two other possibilities: twinning in the crystal and the magnetic breakdown between adjacent orbits. The former is unlikely because similar splits have not been observed in other branches originating from the X and Y domains. The latter is also unlikely because the fourfold split structure is visible over a wide angular range

of $\pm\theta = 0$ – 30° . Hence, we focus on the possibility of the tiny orthorhombic distortion.

The energies of phases II ($I\bar{4}m2$) and III ($I4_122$) are suspected to be very close [56]. In addition, a linear combination of distortions in the $I\bar{4}m2$ and $I4_122$ phases results in the orthorhombic phase of the $F222$ space group. Therefore, if a quantum fluctuation occurred from the $I4_122$ phase to the $I\bar{4}m2$ phase, it would possibly appear as a small distortion to the orthorhombic $F222$ phase. Reference [56] pointed out that the T_{1u} soft phonon mode corresponding to the distortion in the $I\bar{4}m2$ phase may be related to the emergence of superconductivity if the symmetry of the low-temperature phase is $I4_122$. It is possible that the fluctuation of the T_{1u} soft phonon mode freezes and appears as a tiny distortion to the $F222$ symmetry. As far as we infer from the size of the splitting of the γ_{15} branch, this distortion to the orthorhombic structure is so small that it may be difficult to observe, even using methods such as x-ray diffraction. The presence of this small distortion to the $F222$ phase should be verified using high-precision measurements such as NMR.

We also need to supplement our results on structural optimization with the symmetry constrained to the $F222$ space

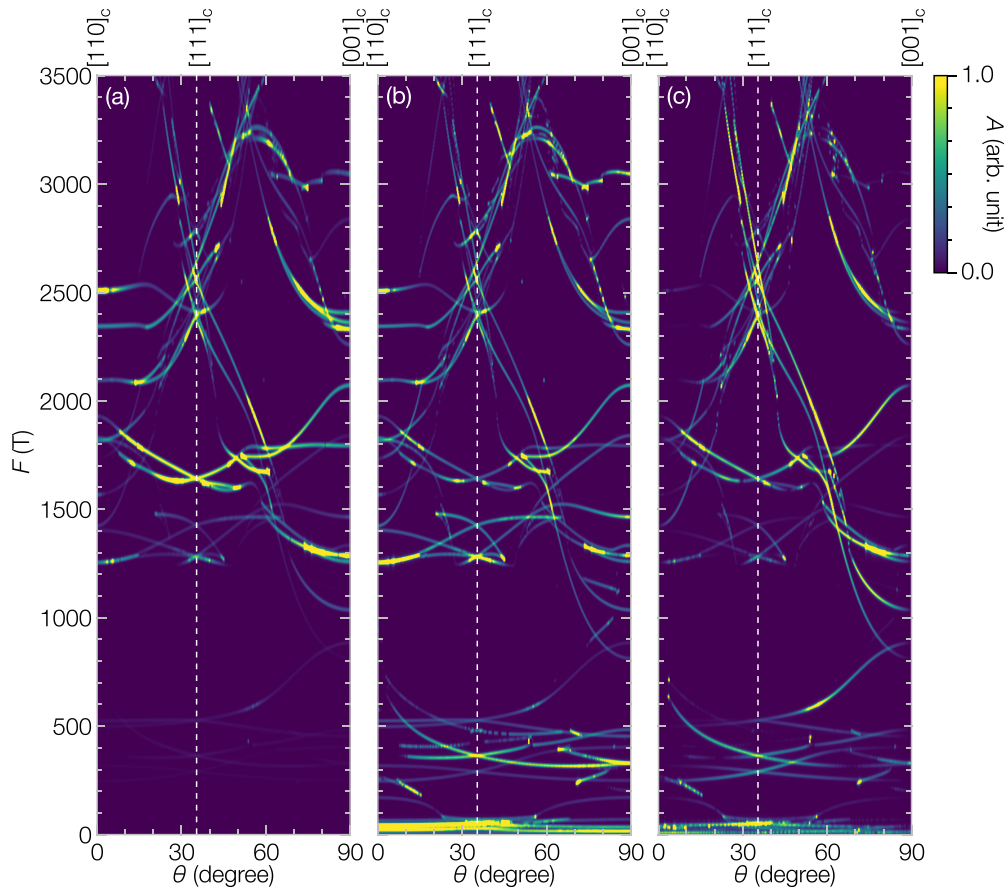


FIG. 13. (a) Angular dependence of the Fourier-transformed spectra calculated for the AC magnetic susceptibility using the modulation method, (b) electrical conductivity, and (c) magnetic torque. A field range of 5–17.5 T, $T_D = 0.1$ K, and $T = 50$ mK were used. Higher harmonics are neglected.

group, which is mentioned in the main text. Because the symmetry breaking to the $F222$ phase, if present, would be expected to be very small, a calculation with insufficient accuracy may easily diminish the stability of the $F222$ phase. Thus, a calculation method superior to the one we have used would possibly enable the $F222$ structure to be stabilized in the calculation. This point would have to be verified in future studies.

APPENDIX D: DISTRIBUTION OF CYCLOTRON EFFECTIVE MASS ON EACH ORBIT

Here, we focus on the m^*/m_b for each orbit of FSs. Figure 14 shows the m^*/m_b of each orbit as a function of F . The observed m^*/m_b 's are distributed near the $\langle m^*/m_b \rangle$. A closer look shows that the small F 's vary relatively widely around $\langle m^*/m_b \rangle$. This is generally because the smaller the F , which is proportional to the cross section of the FS, the more susceptible to effective mass distribution on FSs. In contrast, large F values are concentrated at approximately 2.5, which is smaller than $\langle m^*/m_b \rangle$; this is slightly different from the cases of KOs_2O_6 [75] and CsOs_2O_6 [76], where the m^*/m_b 's are uniformly distributed above and below $\langle m^*/m_b \rangle$. Recalling that we anticipate a large m^*/m_b in FS10, where no oscillation was observed despite the large simulated amplitude, we might suspect that only m^*/m_b in FS10 is exceptionally large among

the FSs [77]. This was completely unexpected because the FSs of $\text{Cd}_2\text{Re}_2\text{O}_7$ consist of intricately hybridized and spin-split bands; thus, there may be no reason for the mass enhancement to be large only at a particular FS [78]. This remains a mystery and should be revisited in future studies.

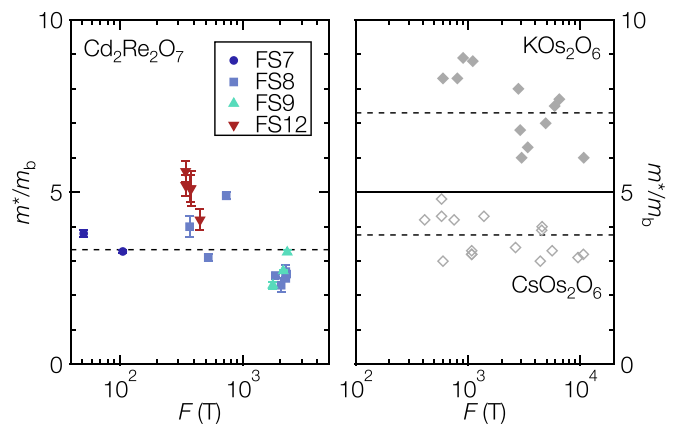


FIG. 14. Orbit-resolved mass enhancement factors m^*/m_b from quantum oscillations as a function of frequency F . Data for KOs_2O_6 [75] and CsOs_2O_6 [76] are shown for comparison. Different symbols are used for different FSs of $\text{Cd}_2\text{Re}_2\text{O}_7$, as indicated by the legend in the figure. The horizontal dashed lines indicate the $\langle m^*/m_b \rangle$ evaluated by γ and γ_b .

TABLE IV. Comparison of the T_c , $\langle m^*/m_b \rangle$, λ_{ep} , λ_{ee} , R_{KW} , and R_W values with related compounds.

Compound	T_c (K)	$\langle m^*/m_b \rangle$	λ_{ep}	λ_{ee}	R_{KW} ($\mu\Omega$ cm mol ² K ² J ⁻²)	R_W
Cd ₂ Re ₂ O ₇	0.97	3.33	0.380	1.41	~10	0.34 [17,19]
KOs ₂ O ₆ [79]	9.6	7.3	1.8 ^a	1.3 ^a	29	0.14
RbOs ₂ O ₆ [79]	6.28	4.38	1.33 ^a	0.65 ^a	16	0.36
CsOs ₂ O ₆ [79]	3.25	3.76	0.78 ^a	1.11 ^a	4.3	0.48
Th ₇ Co ₃ [80]	1.80	1.33	0.56	-0.15 ^b	3.1	0.3
κ -(BEDT-TTF) ₂ Cu(NCS) ₂ [81]	10.4	3.9	0.33 ^c	2.0	- ^d	0.97 ^e

^aThe λ_{ep} value is evaluated using the McMillan formula refined by Allen and Dynes [82] with strong-coupling correction [83]. The λ_{ee} value is evaluated as the residual enhancement of γ .

^bProbably, λ_{ep} is slightly overestimated.

^cThe λ_{ee} value is evaluated using the cyclotron resonance spectra, where only the electron-phonon interaction affects electrons.

^dThe value is $1.8 \times 10^7 \mu\Omega$ cm mol² K² J⁻², which is not appropriate for comparison with the others because dimensionality has a significant effect [84].

^eEvaluated from χ_s and γ from Refs. [85,86], respectively.

APPENDIX E: COMPARISON OF λ_{ep} AND λ_{ee}

It is instructive to compare the obtained values with the related compounds; the T_c , $\langle m^*/m_b \rangle$, λ_{ep} , λ_{ee} , R_{KW} , and R_W values are compared in Table IV with AOs₂O₆ ($A = K, Rb, Cs$), Th₇Co₃, and κ -(BEDT-TTF)₂Cu(NCS)₂. The β -pyrochlores, AOs₂O₆, show rattling-induced superconductivity [79] and share a similarity with Cd₂Re₂O₇ in terms of the $5d$ pyrochlore metallic system. The λ_{ee} and R_{KW} values of Cd₂Re₂O₇ and AOs₂O₆ are comparable. Thus, the strong electron-electron coupling may have an intrinsic origin in the pyrochlore lattice of the $5d$ system. In contrast, λ_{ep} of Cd₂Re₂O₇ is smaller than any of the AOs₂O₆. This is because AOs₂O₆ exhibits enhanced electron-phonon interaction due to the rattling, whereas Cd₂Re₂O₇ does not. In AOs₂O₆, the electron-phonon coupling enhanced by the rattling increases in the order of $A = Cs, Rb$, and K , as

evidenced in λ_{ep} . Hence, the small R_W values are understood because of the enhanced electron-phonon coupling because the R_W decreases in that order [79]. However, the R_W values of RbOs₂O₆ and CsOs₂O₆ are smaller than unity, although they are relatively close to the weak-coupling superconductors. In addition, in Th₇Co₃, a weak-coupling noncentrosymmetric superconductor without rattling, a R_W as small as that of Cd₂Re₂O₇ has been observed [80]. Even in organic superconductors, in which electronic structures are relatively simple, κ -(BEDT-TTF)₂Cu(NCS)₂ has the R_W close to unity [85,86] despite having λ_{ep} and λ_{ee} comparable to and greater than those of Cd₂Re₂O₇, respectively [81]. Therefore, from these examples, we can reasonably conclude that a small value of R_W does not necessarily indicate a small electron-electron interaction and/or a large electron-phonon interaction; another factor that makes R_W small is hidden.

- [1] C. Wu and S.-C. Zhang, Dynamic Generation of Spin-Orbit Coupling, *Phys. Rev. Lett.* **93**, 036403 (2004).
- [2] C. Wu, K. Sun, E. Fradkin, and S.-C. Zhang, Fermi liquid instabilities in the spin channel, *Phys. Rev. B* **75**, 115103 (2007).
- [3] L. Fu, Parity-Breaking Phases of Spin-Orbit-Coupled Metals with Gyrotropic, Ferroelectric, and Multipolar Orders, *Phys. Rev. Lett.* **115**, 026401 (2015).
- [4] S. Hayami, M. Yatsushiro, Y. Yanagi, and H. Kusunose, Classification of atomic-scale multipoles under crystallographic point groups and application to linear response tensors, *Phys. Rev. B* **98**, 165110 (2018).
- [5] H. Watanabe and Y. Yanase, Group-theoretical classification of multipole order: Emergent responses and candidate materials, *Phys. Rev. B* **98**, 245129 (2018).
- [6] S. Hayami, Y. Yanagi, H. Kusunose, and Y. Motome, Electric Toroidal Quadrupoles in the Spin-Orbit-Coupled Metal Cd₂Re₂O₇, *Phys. Rev. Lett.* **122**, 147602 (2019).
- [7] V. Kozii and L. Fu, Odd-Parity Superconductivity in the Vicinity of Inversion Symmetry Breaking in Spin-Orbit-Coupled Systems, *Phys. Rev. Lett.* **115**, 207002 (2015).
- [8] Y. Wang, G. Y. Cho, T. L. Hughes, and E. Fradkin, Topological superconducting phases from inversion symmetry breaking order in spin-orbit-coupled systems, *Phys. Rev. B* **93**, 134512 (2016).
- [9] F. Wu and I. Martin, Nematic and chiral superconductivity induced by odd-parity fluctuations, *Phys. Rev. B* **96**, 144504 (2017).
- [10] S. Sumita, T. Nomoto, and Y. Yanase, Multipole Superconductivity in Nonsymmorphic Sr₂IrO₄, *Phys. Rev. Lett.* **119**, 027001 (2017).
- [11] S. Sumita and Y. Yanase, Superconductivity induced by fluctuations of momentum-based multipoles, *Phys. Rev. Research* **2**, 033225 (2020).
- [12] Z. Hiroi, J. Yamaura, T. C. Kobayashi, Y. Matsubayashi, and D. Hirai, Pyrochlore oxide superconductor Cd₂Re₂O₇ revisited, *J. Phys. Soc. Jpn.* **87**, 024702 (2018).
- [13] M. Subramanian, G. Aravamudan, and G. Subba Rao, Oxide pyrochlores â A review, *Prog. Solid State Chem.* **15**, 55 (1983).
- [14] J. Yamaura and Z. Hiroi, Low temperature symmetry of pyrochlore oxide Cd₂Re₂O₇, *J. Phys. Soc. Jpn.* **71**, 2598 (2002).
- [15] J. P. Castellan, B. D. Gaulin, J. van Duijn, M. J. Lewis, M. D. Lumsden, R. Jin, J. He, S. E. Nagler, and D. Mandrus, Structural ordering and symmetry breaking in Cd₂Re₂O₇, *Phys. Rev. B* **66**, 134528 (2002).
- [16] H. Sakai, H. Kato, S. Kambe, R. E. Walstedt, H. Ohno, M. Kato, K. Yoshimura, and H. Matsuhata, Low-temperature structural change and magnetic anomaly in superconducting Cd₂Re₂O₇, *Phys. Rev. B* **66**, 100509(R) (2002).

- [17] O. Vyaselev, K. Arai, K. Kobayashi, J. Yamazaki, K. Kodama, M. Takigawa, M. Hanawa, and Z. Hiroi, Superconductivity and Magnetic Fluctuations in $\text{Cd}_2\text{Re}_2\text{O}_7$ via Cd Nuclear Magnetic Resonance and Re Nuclear Quadrupole Resonance, *Phys. Rev. Lett.* **89**, 017001 (2002).
- [18] R. Jin, J. He, J. R. Thompson, M. F. Chisholm, B. C. Sales, and D. Mandrus, Fluctuation effects on the physical properties of $\text{Cd}_2\text{Re}_2\text{O}_7$ near 200 K, *J. Phys.: Condens. Matter* **14**, L117 (2002).
- [19] Z. Hiroi, M. Hanawa, Y. Muraoka, and H. Harima, Correlations and semimetallic behaviors in pyrochlore oxide $\text{Cd}_2\text{Re}_2\text{O}_7$, *J. Phys. Soc. Jpn.* **72**, 21 (2003).
- [20] S. Tajima, D. Hirai, Y. Kinoshita, M. Tokunaga, K. Akiba, T. C. Kobayashi, H. T. Hirose, and Z. Hiroi, Domain control by adjusting anisotropic stress in pyrochlore oxide $\text{Cd}_2\text{Re}_2\text{O}_7$, *J. Phys. Soc. Jpn.* **89**, 114711 (2020).
- [21] J. Labbé and J. Friedel, Electron instability and crystalline phase transformations of V_3Si type compounds at low temperatures, *J. Phys. (France)* **27**, 153 (1966).
- [22] E. Fradkin, S. A. Kivelson, M. J. Lawler, J. P. Eisenstein, and A. P. Mackenzie, Nematic fermi fluids in condensed matter physics, *Annu. Rev. Condens. Matter Phys.* **1**, 153 (2010).
- [23] In fact, by definition, phases II and III can be regarded as kinds of electronic nematic order phases in that they break the threefold symmetry of phase I while keeping the translational invariance and metallic state [22].
- [24] Z. Hiroi, J.-I. Yamaura, Y. Muraoka, and M. Hanawa, Second phase transition in pyrochlore oxide $\text{Cd}_2\text{Re}_2\text{O}_7$, *J. Phys. Soc. Jpn.* **71**, 1634 (2002).
- [25] I. A. Sergienko and S. H. Curnoe, Structural order parameter in the pyrochlore superconductor $\text{Cd}_2\text{Re}_2\text{O}_7$, *J. Phys. Soc. Jpn.* **72**, 1607 (2003).
- [26] K. J. Kapcia, M. Reedyk, M. Hajjalamdari, A. Ptok, P. Piekarczyk, A. Schulz, F. S. Razavi, R. K. Kremer, and A. M. Oleś, Discovery of a low-temperature orthorhombic phase of the $\text{Cd}_2\text{Re}_2\text{O}_7$ superconductor, *Phys. Rev. Research* **2**, 033108 (2020).
- [27] J.-I. Yamaura, K. Takeda, Y. Ikeda, N. Hirao, Y. Ohishi, T. C. Kobayashi, and Z. Hiroi, Successive spatial symmetry breaking under high pressure in the spin-orbit-coupled metal $\text{Cd}_2\text{Re}_2\text{O}_7$, *Phys. Rev. B* **95**, 020102(R) (2017).
- [28] Y. Matsubayashi, D. Hirai, M. Tokunaga, and Z. Hiroi, Formation and control of twin domains in the pyrochlore oxide $\text{Cd}_2\text{Re}_2\text{O}_7$, *J. Phys. Soc. Jpn.* **87**, 104604 (2018).
- [29] Y. Matsubayashi, K. Sugii, D. Hirai, Z. Hiroi, T. Hasegawa, S. Sugiura, H. T. Hirose, T. Terashima, and S. Uji, Coexistence of odd-parity and even-parity order parameters in the multipole order phase of the spin-orbit coupled metal $\text{Cd}_2\text{Re}_2\text{O}_7$, *Phys. Rev. B* **101**, 205133 (2020).
- [30] R. Jin, J. He, S. McCall, C. S. Alexander, F. Drymiotis, and D. Mandrus, Superconductivity in the correlated pyrochlore $\text{Cd}_2\text{Re}_2\text{O}_7$, *Phys. Rev. B* **64**, 180503(R) (2001).
- [31] Z. Hiroi and M. Hanawa, Superconducting properties of the pyrochlore oxide $\text{Cd}_2\text{Re}_2\text{O}_7$, *J. Phys. Chem. Solids* **63**, 1021 (2002).
- [32] K. Momma and F. Izumi, VESTA3 for three-dimensional visualization of crystal, volumetric and morphology data, *J. Appl. Cryst.* **44**, 1272 (2011).
- [33] S. Uji, S. Sugiura, H. T. Hirose, T. Terashima, Y. Matsubayashi, D. Hirai, Z. Hiroi, and T. Hasegawa, Anomalous changes of electric quadrupole order at low temperatures in the spin-orbit coupled metal $\text{Cd}_2\text{Re}_2\text{O}_7$, *Phys. Rev. B* **102**, 155131 (2020).
- [34] J. C. Petersen, M. D. Caswell, J. S. Dodge, I. A. Sergienko, J. He, R. Jin, and D. Mandrus, Nonlinear optical signatures of the tensor order in $\text{Cd}_2\text{Re}_2\text{O}_7$, *Nat. Phys.* **2**, 605 (2006).
- [35] J. W. Harter, Z. Y. Zhao, J.-Q. Yan, D. G. Mandrus, and D. Hsieh, A parity-breaking electronic nematic phase transition in the spin-orbit coupled metal $\text{Cd}_2\text{Re}_2\text{O}_7$, *Science* **356**, 295 (2017).
- [36] S. Di Matteo and M. R. Norman, Nature of the tensor order in $\text{Cd}_2\text{Re}_2\text{O}_7$, *Phys. Rev. B* **96**, 115156 (2017).
- [37] Y. Matsubayashi, K. Sugii, H. T. Hirose, D. Hirai, S. Sugiura, T. Terashima, S. Uji, and Z. Hiroi, Split fermi surfaces of the spinorbit-coupled metal $\text{Cd}_2\text{Re}_2\text{O}_7$ probed by de Haas-van Alphen effect, *J. Phys. Soc. Jpn.* **87**, 053702 (2018).
- [38] S.-W. Huang, H.-T. Jeng, J.-Y. Lin, W. J. Chang, J. M. Chen, G. H. Lee, H. Berger, H. D. Yang, and K. S. Liang, Electron structure of pyrochlore $\text{Cd}_2\text{Re}_2\text{O}_7$, *J. Phys.: Condens. Matter* **21**, 195602 (2009).
- [39] D. Shoenberg, *Magnetic Oscillations in Metals*, Cambridge Monographs on Physics (Cambridge University Press, Cambridge, 1984).
- [40] A. I. Liechtenstein, V. I. Anisimov, and J. Zaanen, Density-functional theory and strong interactions: Orbital ordering in Mott-Hubbard insulators, *Phys. Rev. B* **52**, R5467 (1995).
- [41] P. Giannozzi, O. Andreussi, T. Brumme, O. Bunau, M. B. Nardelli, M. Calandra, R. Car, C. Cavazzoni, D. Ceresoli, M. Cococcioni, N. Colonna, I. Carnimeo, A. D. Corso, S. de Gironcoli, P. Delugas, R. A. D. Jr., A. Ferretti, A. Floris, G. Fratesi, G. Fugallo *et al.*, Advanced capabilities for materials modeling with Quantum ESPRESSO, *J. Phys.: Condens. Matter* **29**, 465901 (2017).
- [42] D. R. Hamann, <https://github.com/oncvpsp/oncvpsp>.
- [43] D. R. Hamann, Optimized norm-conserving Vanderbilt pseudopotentials, *Phys. Rev. B* **88**, 085117 (2013).
- [44] M. Schlipf and F. Gygi, Optimization algorithm for the generation of ONCV pseudopotentials, *Comput. Phys. Commun.* **196**, 36 (2015).
- [45] P. Scherpelz, M. Govoni, I. Hamada, and G. Galli, Implementation and validation of fully relativistic gw calculations: Spin-orbit coupling in molecules, nanocrystals, and solids, *J. Chem. Theory Comput.* **12**, 3523 (2016).
- [46] J. P. Perdew, K. Burke, and M. Ernzerhof, Generalized Gradient Approximation Made Simple, *Phys. Rev. Lett.* **77**, 3865 (1996).
- [47] G. Pizzi, V. Vitale, R. Arita, S. Blügel, F. Freimuth, G. Géranton, M. Gibertini, D. Gresch, C. Johnson, T. Koretsune, J. Ibañez-Azpiroz, H. Lee, J. M. Lihm, D. Marchand, A. Marrazzo, Y. Mokrousov, J. I. Mustafa, Y. Nohara, Y. Nomura, L. Paulatto *et al.*, Wannier90 as a community code: new features and applications, *J. Phys.: Condens. Matter* **32**, 165902 (2020).
- [48] P. M. C. Rourke and S. R. Julian, Numerical extraction of de Haas-van Alphen frequencies from calculated band energies, *Comput. Phys. Commun.* **183**, 324 (2012).
- [49] I. Timrov, N. Marzari, and M. Cococcioni, Hubbard parameters from density-functional perturbation theory, *Phys. Rev. B* **98**, 085127 (2018).
- [50] J. He, Metallic Ferroelectricity and Superconductivity in the Transition Metal Oxide Pyrochlore $\text{Cd}_2\text{Re}_2\text{O}_7$, PhD diss., University of Tennessee, 2004, original paper misprints Wyckoff sites.

- [51] M. M. Miller and R. Reifenberger, Magnetic breakdown and the de Haas–van Alphen effect in $\text{Hg}_{1-x}\text{Fe}_x\text{Se}$, *Phys. Rev. B* **38**, 3423 (1988).
- [52] N. Kimura, H. Sano, M. Shirakawa, A. Ochiai, H. Funashima, and H. Harima, Orbital crossing on split fermi surfaces in non-centrosymmetric Yb_4Sb_3 , *J. Phys. Soc. Jpn.* **87**, 114708 (2018).
- [53] The $\text{O}(2_1)$ site corresponds to the $\text{O}(4)$ site in phase III.
- [54] M. T. Weller, R. W. Hughes, J. Rooke, C. S. Knee, and J. Reading, The pyrochlore family a potential panacea for the frustrated perovskite chemist, *Dalton Trans.* **19**, 3032 (2004).
- [55] J. He, R. Jin, B. C. Chakoumakos, J. S. Gardner, D. Mandrus, and T. M. Tritt, Crystal growth, structure, and stoichiometry of the superconducting pyrochlore $\text{Cd}_2\text{Re}_2\text{O}_7$, *J. Electron. Mater.* **36**, 740 (2007).
- [56] I. A. Sergienko, V. Keppens, M. McGuire, R. Jin, J. He, S. H. Curnoe, B. C. Sales, P. Blaha, D. J. Singh, K. Schwarz, and D. Mandrus, Metallic “Ferroelectricity” in the Pyrochlore $\text{Cd}_2\text{Re}_2\text{O}_7$, *Phys. Rev. Lett.* **92**, 065501 (2004).
- [57] D. J. Singh, P. Blaha, K. Schwarz, and J. O. Sofo, Electronic structure of the pyrochlore metals $\text{Cd}_2\text{Os}_2\text{O}_7$ and $\text{Cd}_2\text{Re}_2\text{O}_7$, *Phys. Rev. B* **65**, 155109 (2002).
- [58] H. Harima, Electronic bandstructures on 5d-transition metal pyrochlore: $\text{Cd}_2\text{Re}_2\text{O}_7$ and $\text{Cd}_2\text{Os}_2\text{O}_7$, *J. Phys. Chem. Solids* **63**, 1035 (2002).
- [59] I. V. Solov'yev, Effects of crystal structure and on-site Coulomb interactions on the electronic and magnetic structure of $\text{A}_2\text{Mo}_2\text{O}_7$ ($A = \text{Y}, \text{Gd}, \text{and Nd}$) pyrochlores, *Phys. Rev. B* **67**, 174406 (2003).
- [60] M. Brühwiler, S. M. Kazakov, J. Karpinski, and B. Batlogg, Mass enhancement, correlations, and strong-coupling superconductivity in the β -pyrochlore KOs_2O_6 , *Phys. Rev. B* **73**, 094518 (2006).
- [61] N. W. Ashcroft and N. D. Mermin, *Solid State Physics* (Saunders College Publishing, Philadelphia, 1976).
- [62] For instance, $F = 1824\text{T}$ of the γ_{10} frequency at $B \parallel \langle 111 \rangle$ corresponds to $k_F^{-1} \simeq 6.0 \text{ \AA}$ if we assume a circular orbit shape.
- [63] For example, the heavy Fermion material YbNi_2 has been observed to have a huge specific heat coefficient $\gamma = 573 \text{ mJ mol}^{-1}\text{K}^2$ [87], but the band specific heat coefficient γ_b calculated by the DFT and DFT + U methods are reported as 29.937 and 28.270 $\text{mJ mol}^{-1}\text{K}^2$, respectively [88].
- [64] S. Koshino, Scattering of electrons by the thermal motion of impurity ions, *Prog. Theor. Exp. Phys.* **24**, 484 (1960).
- [65] P. L. Taylor, Changes in electrical resistance caused by incoherent electron-phonon scattering, *Phys. Rev.* **135**, A1333 (1964).
- [66] K. Kadowaki and S. Woods, Universal relationship of the resistivity and specific heat in heavy-Fermion compounds, *Solid State Commun.* **58**, 507 (1986).
- [67] H. Sakai, Y. Tokunaga, S. Kambe, K. Kitagawa, H. Murakawa, K. Ishida, H. Ohno, M. Kato, K. Yoshimura, and R. E. Walstedt, Decrease in ^{111}Cd knight shift in superconducting $\text{Cd}_2\text{Re}_2\text{O}_7$: Evidence for spin-singlet pairing, *J. Phys. Soc. Jpn.* **73**, 2940 (2004).
- [68] F. Razavi, Y. Rohanizadegan, M. Hajialamdari, M. Reedyk, R. Kremer, and B. Mitrovi, The effect of quasiparticle self-energy on $\text{Cd}_2\text{Re}_2\text{O}_7$ superconductor, *Can. J. Phys.* **93**, 1646 (2015).
- [69] K. G. Wilson, The renormalization group: Critical phenomena and the Kondo problem, *Rev. Mod. Phys.* **47**, 773 (1975).
- [70] W. L. McMillan, Transition temperature of strong-coupled superconductors, *Phys. Rev.* **167**, 331 (1968).
- [71] J. W. Garland and K. H. Bennemann, Theory for the pressure dependence of T_c for narrow-band superconductors, *AIP Conf. Proc.* **4**, 255 (1972).
- [72] T. Radzyński and A. Łusakowski, Influence of spin-orbit interaction on band structure and elastic properties of PbTe , *Acta Phys. Pol. A* **116**, 954 (2009).
- [73] I. V. Solov'yev, P. H. Dederichs, and V. I. Anisimov, Corrected atomic limit in the local-density approximation and the electronic structure of d impurities in Rb , *Phys. Rev. B* **50**, 16861 (1994).
- [74] M. Cococcioni and S. de Gironcoli, Linear response approach to the calculation of the effective interaction parameters in the LDA + U method, *Phys. Rev. B* **71**, 035105 (2005).
- [75] T. Terashima, N. Kurita, A. Kiswandhi, E.-S. Choi, J. S. Brooks, K. Sato, J.-I. Yamaura, Z. Hiroi, H. Harima, and S. Uji, Large and homogeneous mass enhancement in the rattling-induced superconductor KOs_2O_6 , *Phys. Rev. B* **85**, 180503(R) (2012).
- [76] T. Terashima, S. Uji, Y. Nagao, J. Yamaura, Z. Hiroi, and H. Harima, Fermi surface in the superconducting β -pyrochlore oxide CsOs_2O_6 , *Phys. Rev. B* **77**, 064509 (2008).
- [77] Because the carrier number in FS10 is 11.5% of the total, assuming $m^*/m_b = 2.5$ for the other carriers, the upper limit of m^*/m_b for FS10 is estimated to be ~ 10 .
- [78] For reference, in KOs_2O_6 and CsOs_2O_6 , the m^*/m_b distribute within only $\pm 20\%$ around the $\langle m^*/m_b \rangle$.
- [79] Y. Nagao, J.-I. Yamaura, H. Ogusu, Y. Okamoto, and Z. Hiroi, Rattling-induced superconductivity in the β -pyrochlore oxides AOs_2O_6 , *J. Phys. Soc. Jpn.* **78**, 064702 (2009).
- [80] M. Sahakyan and V. H. Tran, Physical properties and electronic band structure of noncentrosymmetric Th_7Co_3 superconductor, *J. Phys.: Condens. Matter* **28**, 205701 (2016).
- [81] T. Kawamoto and T. Mori, Many-body effect on the superconducting transition temperature in layered organic superconductors, *Phys. Rev. B* **74**, 212502 (2006).
- [82] P. B. Allen and R. C. Dynes, Transition temperature of strong-coupled superconductors reanalyzed, *Phys. Rev. B* **12**, 905 (1975).
- [83] F. Marsiglio and J. P. Carbotte, Strong-coupling corrections to Bardeen-Cooper-Schrieffer ratios, *Phys. Rev. B* **33**, 6141 (1986).
- [84] A. Jacko, J. Fjærestad, and B. Powell, A unified explanation of the KadowakiWoods ratio in strongly correlated metals, *Nat. Phys.* **5**, 422 (2009).
- [85] K. Kanoda, Metal–insulator transition in $\kappa\text{-(ET)}_2\text{X}$ and $(\text{DCNQI})_2\text{M}$: Two contrasting manifestation of electron correlation, *J. Phys. Soc. Jpn.* **75**, 051007 (2006).
- [86] B. Andraka, J. S. Kim, G. R. Stewart, K. D. Carlson, H. H. Wang, and J. M. Williams, Specific heat in high magnetic field of $\kappa\text{-di[bis(ethylenedithio)tetrathiafulvalene]-di(thiocyano)cuprate}$ [$\kappa\text{-(ET)}_2\text{Cu(NCS)}_2$]: Evidence for strong-coupling superconductivity, *Phys. Rev. B* **40**, 11345 (1989).
- [87] D. Rojas, L. Fernández Barquín, C. Echevarria-Bonet, and J. Rodríguez Fernández, YbNi_2 : A heavy fermion ferromagnet, *Solid State Commun.* **152**, 1834 (2012).
- [88] Y. E and B.-N. Wu, First-principles study of the electronic structure of heavy fermion YbNi_2 , *J. Supercond. Novel Magn.* **27**, 735 (2014).